The response of wind drag to underlying swell slope

William L. Peirson, Hubert Branger, Jean-Paul Giovanangeli, Michael Banner

THE UNIVERSITY OF NEW SOUTH WALES
SCHOOL OF CIVIL AND ENVIRONMENTAL ENGINEERING
WATER RESEARCH LABORATORY

THE RESPONSE OF WIND DRAG TO UNDERLYING SWELL SLOPE

WRL Research Report 223 December 2004

by

William L Peirson
Hubert Branger (CNRS-Université de la Méditerranée)
Jean-Paul Giovanangeli (CNRS-Université de la Méditerranée)
Michael L. Banner (School of Mathematics, University of New South Wales)

Water Research Laboratory
School of Civil and Environmental Engineering
University of New South Wales ABN 57 195 873 179
King Street
Manly Vale NSW 2093 Australia

Telephone: +61 (2) 9949 4488
Facsimile: +61 (2) 9949 4188

Research Report	223
Report Status	Final
Date of Issue	December 2004

ISBN 85824 030/2

ABSTRACT

Lack of knowledge of the development of momentum flux response to wave field steepness is hampering the development of more quantitative understanding of wind-induced energy fluxes which are critical to prediction of maritime safety under severe wave conditions.

Laboratory experiments were undertaken to determine total drag response to mean swell steepness. It was established that : the introduction of monochromatic low frequency waves beneath microscale waves disrupts the microscale in such a way that the total stress borne by the surface can fall by up to 20%. Behaviour is systematic in terms of mean low frequency wave steepness. Once the low frequency waves achieve a sufficient mean steepness (~0.15), their presence augments the total stress with a very strong response observed above a mean steepness of 0.20. Consistent behaviour was observed across a range of wave scales and wind forcing.

Consistent development of mean spectral energy in the frequency range 8 to 30 Hz was also observed which may have implications for remote sensing of the ocean.

Limited form drag measurements obtained during this study show consistent development of form drag with mean wave steepness that has not previously been observed.

A tentative qualitative description of the development of drag over the ocean is developed. Future studies which would clarify existing uncertainty regarding wind-induced momentum and energy fluxes to the surface of the open ocean are described.

CONTENTS

LIST OF TABLES

LIST OF FIGURES

1. INTRODUCTION

Adequate prediction of the total drag generated by wind over the open ocean is fundamental to adequate descriptions of all air-sea interaction processes especially wind wave growth and the behaviours of the atmospheric and aqueous boundary layers. Significant gaps in our understanding of the behaviour of total drag remain with investigators divided on appropriate schemes to reconcile observed fetch dependencies (compare Donelan et al., 1993 and Jones and Toba, 1995).

It is has been shown that the transition of waves from the non-breaking to breaking state trigger a strong response in drag behaviour. Banner (1990) showed that the total wind-induced momentum flux approximately doubled when a slight increase in mean wave steepness (*ak*) shifted the wave field from an unbroken to a continuously breaking state for two wave frequency conditions. This result was unintentionally corroborated by an earlier study by Bliven et al. (1986) who showed rapid increases in drag over waves of a single frequency as *ak* increased above a value of 0.2.

The steepest sea states are those of strongest wind forcing and consequently those of greatest concern in terms of maritime safety and offshore structural loading. Numerical spectral representations are now focussing on the role of air flow separation in the development of total drag (see, for example, Makin and Kudryavtsev, 2002) and the critical role of steep wave behaviour. However, there have been very few controlled investigations that have been directly examined the development of drag over steep wind waves.

Recent papers by Peirson et al. (2003) and Peirson and Belcher (2004) have shown a strong and systematic relationship between energy flux and momentum flux from opposing and co-flowing winds to waves as a function of mean wave steepness. However, better intrinsic understanding of wave energy fluxes will not be possible until the response of total drag from the wind to the characteristics of steep wave fields is more clearly defined.

During this investigation, we have undertaken controlled experiments on wind-forced, laboratory wave fields. By carefully varying the mean steepness of an underlying paddle-generated wave field, we have carefully examined the development of total drag as the wave steepness is increased across a range of wind and wave conditions. A preliminary investigation of wind-induced form drag and wind energy input for a single wind and wave condition is also reported.

In the open ocean, swell is defined as incident low frequency waves that have been generated remotely and not by the local wind. In this report, we will refer to monochromatic, paddle

generated waves as *swell* to distinguish them from waves generated in a laboratory tank by direct action of the wind. Our so-called laboratory *swell* have higher frequencies (typically > 0.5Hz) than their ocean counterparts (frequencies typically < 0.12Hz). We also know that there are important differences between open ocean swell spectra and those of monochromatic wave fields. Extrapolation from laboratory to open ocean must be undertaken with caution.

2. PREVIOUS STUDIES

Bliven, Hwang and Long (1986)

If monochromatic, non-breaking unidirectional wave fields are subjected to moderate wind forcing, Bliven *et al.,* 1986 have shown that non-linear interactions of the monochromatic wave are suppressed. The investigation by Bliven *et al.* (1986) was not specifically directed at investigating wind-induced momentum and energy fluxes to the wave field. However, their investigation is relevant to this study because their measurements of stress in the air showed little change in total wind stress up to a value of mean wave steepness of approximately 0.15 of waves with 2.0Hz frequency.

Donelan (1987)

It is well established that the addition of low-frequency mechanically generated waves will attenuate an existing wind-wave field in a laboratory tank. This appears to have first been reported by Mitsuyasu (1966). Phillips and Banner (1974) performed further experiments and developed a model for the observed attenuation. Donelan (1987) completed quantitative experiments on the wind input to the wind waves at two wind speeds and three low frequency wave steepnesses. He concluded that the normalised rate of wind input to the wind waves remained unchanged with the addition of the paddle waves and that the reasons for suppression of the wind waves was unclear. While not discussed explicitly, Donelan also observed an increase in mean wind speed with the addition of the paddle waves. This result also suggests that the presence of monochromatic swell which directly implies are reduction in drag of the surface.

Banner (1990)

Airflow behaviour over breaking waves had been observed to be significantly different from that over unbroken waves by Banner and Melville (1976). The study of Banner (1990) investigated the changes in total drag and form drag over waves at the transition to microscale breaking over waves of frequencies of 2.85 and 3.35Hz. The form drag was obtained from air pressure/wave slope correlations.

It was observed that the form drag and total drag both approximately doubled with the transition to the breaking condition. However, the ratio of form drag to total drag remained approximately the same for steep non-breaking and continuous breaking wave conditions.

3. MEASUREMENTS

3.1 Experimental Facility

Our investigations were undertaken in the IRPHE tank of the CNRS-Université de la Méditerranée at Marseille in France. This is a large wind-wave facility composed of a recirculating air flow channel with a 40 m long, 3.2 m wide, 1.6 m high test section and a 40 m long, 2.6 m wide, up to 1 m deep water tank (Figure 1). Two water pumps can create following or opposite currents up to 10 cm/s in the full water reservoir. During these experiments, the pumps remained off.

A submerged wavemaker can generate regular and random water waves in the frequency range from 0.5 to 2 Hz. It consists of an oscillating plate located at the bottom of a cavity below the air-water flow junction device (Figure 1) and is computer controlled by an electro-hydraulic motor. The upwind end of the tank is specially profiled to ensure minimum disturbance to either the generation of mechanical waves or the turbulent boundary layer in the air flow above the waves.

At the downwind end of the tank, a permeable absorbing beach has been installed to minimise wave reflection.

The fan can generate winds up to 14 m/s in the test section. The air flow channel includes divergent and convergent sections, turbulence grids and a slight enlargement of the test section specially designed to obtain a low-turbulence homogeneous flow at the entrance of the test section. An important feature of this tank is the careful profiling of the roof which is designed to create a "constant-flux" boundary layer at the water surface along the length of the tank.

During this study, paddle-generated swell were exposed to varying degrees of wind forcing. Mean wave steepness will be varied using the wave generator. Waves are generated by a controlled random generator at one end of the tank. During these investigations, the generated spectrum consisted only of monochromatic waves to enable the contribution of the swell and high frequency wind waves to be distinguished.

Observations were taken at a fetch of 10m from the upwind end of the tank. The array of instruments used during the measurements are shown in Figure 2.

3.2 Wave, wind and pressure measurements and processing

Wave measurements and processing

Waves were monitored using two capacitance wave probes at Δx=50 mm spacing aligned along the axis of the tank. Each probe was digitized at a rate of 300 Hz, and the data were stored for subsequent processing.

The local slope of the waves $\eta_x(t)$ were computed using two methods :

$$\eta_x(t)=\frac{\eta_1(t)-\eta_2(t)}{\Delta x} \tag{1}$$

$$\eta_x(t)=\frac{\eta_1(t+\delta t)-\eta_1(t)}{c\,\delta t} \tag{2}$$

where η is the water surface elevation at a particular probe and c is the phase speed given by:

$$c=\frac{\omega_p}{k_p} \tag{3}$$

ω_p was detected through Fourier analysis (maximum spectral peak detection).

k_p was computed using the two methods described in equations 4 and 5:

$$k_p=\sqrt{\frac{max\,(slope\ spectrum)}{max\,(amplitude\ spectrum)}} \tag{4}$$

$$k_p=\frac{\Delta(\varphi(f_p))}{\Delta x} \tag{5}$$

where $\Delta(\varphi(f_p))$ is the spectral phase shift, at the peak frequency, between the two wave gauge time series.

In order to compute steepness of waves, we undertook zero-up crossing wave time series analysis as follows:

1. The wave records were filtered to exclude wave energy at frequencies greater than $3f_p$.
2. Waves were extracted from up-zero crossing analysis
3. The wave amplitude was calculated as half the difference in height between the maximum and minimum water level recording during the transit of each wave.
4. The steepness of each transit wave was computed by multiplied the wave amplitude by

the wave number of the dominant wave k_p

5. The mean wave steepness is equal to the mean of all the steepnesses computed for each wave.
6. The maximum forward wave slope for each transit wave was calculated by founding the maximum positive slope for each individual wave.

Wind and Total Stress Measurements

X-probe hot wires were used to measure the total stress applied to the water surface. These were amplified and digitised at a rate of 300Hz per channel in blocks of 5 minutes. For each block, the mean velocity was computed and then the fluctuating velocity components were used to calculate the mean turbulent stress in the customary manner. A pitot tube was used to monitor any drift in the hot wires during their operation.

Prior to testing, we carefully checked that a constant turbulent stress layer existed immediately above the water surface at our test location. The developed layer thickness is shown at 10m/s wind speed in Figure 3. At all lower wind speeds, the constant stress layer thickness will be thicker than this and all measurements were taken within 100mm of the mean water surface.

For testing steep (that is, mean steepness AK>0.20) swell at a wind speed of $10ms^{-1}$, it was necessary to raise the position of the hot wires above 100mm elevation to avoid the impact of large waves. Potentially, for these conditions, the measured friction velocity may have been slightly too low. No measurements were taken at elevations greater than 133mm therefore our indicated values will not underestimate the total stress under such conditions by more than 10%.

Static Pressure and Form Drag Measurements

To complement the total stress measurements, measurements of the static pressure above the waves were also undertaken.

The bleed-type pressure sensor of Giovanangeli and Chambaud (1987) was used as a total tube (Figure 2) and deployed at the same level and in close proximity to the X-wires. The static pressure was obtained by subtracting the dynamic pressure (calculated from the X-wire measurements from the total pressure measured by the total tube.

Preliminary testing showed that pressure fluctuations in the tank were contaminated by noise

from the wave generator. Consequently, during static pressure measurement testing the paddle was arrested prior to data capture.

The static pressure measurements were obtained at a fixed elevation and no corrections were made to extrapolate these to the surface. The form drag of the waves was obtained by computing the by computing the mean value of the product of the static pressure multiplied by wave slope via:

$$\tau_{form} = \frac{1}{T} \int_0^T P_s(t) \frac{\partial \eta(t)}{\partial x} dt \tag{6}$$

Coherency and phase shift between pressure and slope were calculated in the spectral domain. A significant coherency (>0.6) at the swell frequency indicates a high coupling between air pressure fluctuations and waves. A phase shift greater than 45° indicates a significant contribution of the form drag to wave amplification.

4. RESULTS AND DISCUSSION

Steep wave trains are unstable in a number of modes (Benjamin-Feir, 1967, Kharif and Ramamonjiarisoa, 1988, Melville, 1982). Our decision to undertake the experiments a substantial distance from the end of the tank made our test conditions vulnerable to these instabilities. However, as observed by Bliven *et al.*(1986) the imposition of wind tends to suppress these instabilities. Therefore, our test conditions were selected to minimise group formation and lateral variations in the wave forms. We found that if the wind forcing was too light, the instabilities would dominate the steep paddle waves making them far from monochromatic at the test section. Equally, if the wind was too strong, the spectra downshift in the peak frequency of wind-generated waves would become so rapid that the two frequency bands would coalesce.

Four experiments were undertaken as summarised in Table 1.

Table 1. Experiment Conditions

monochromatic wave frequency f_s [Hz]	U [m/s]	u* (AK=0.0) [m/s]	z0 (AK=0.0) [mm]	No. of total stress measure-ments	No of form drag measurements
2.0	6.0	0.257	0.10	20	0
1.6	8.0	0.375	0.13	28	0
1.4	6.0	0.265	0.19	30	20
1.4	10.0	0.505	0.24	29	0

4.1 Wave Field Characteristics

Representative spectra for each case are presented in Figures 4 and 5. The following observations can be made:

1. Wind-wave activity is suppressed as the swell energy develops (Mitsuyasu, 1966, Phillips and Banner, 1974).
2. There is a spectral upshift in the peak energy of the wind-waves with increasing swell steepness (Donelan, 1987).
3. Non-linear spectral contributions from both the swell and the wind waves.
4. Development of spectral sidebands with increasing swell steepness – as would be expected, these effects are most pronounced for the higher frequency paddle waves.

Spectral analysis has its limitations in describing steep, wind-forced waves. Therefore, we have also undertaken some preliminary zero-crossing analysis as described in Section 3.2. Note that this analysis does not distinguish between swell and local wind waves. Figure 6 shows the distributions of local mean wave steepness for all waves. As anticipated, at the

lowest swell steepness, significant contributions from the wind waves are apparent. Figure 7 shows the distributions in forward face slope at representative values of mean AK.

We attempted to document breaking probability in three ways:

1. We computed the proportion of waves having maximum leeward face slope greater than 0.5. This approach is comparable with that of Banner (1990). The results are contaminated by the wind waves at low swell steepness. However, the forward face slopes seem to be considerably less than observed by Banner (1990). At AK=0.25, we visually observed the waves to be almost continuously breaking and if the Banner (1990) results were extrapolated to this scale, we would expect to see almost 100% of waves having a forward face slope greater than 0.5. This is not the case and we are unable to comment on this matter further except to acknowledge a possible scale dependence of leeward face slope of actively breaking waves which requires further investigation.
2. We observed that breaking was accompanied by characteristic high frequency wave generation in the vicinity of the break point. We selected a frequency band between 8 and 30 Hz. At these frequencies we had observed no significant contribution of harmonics from swell non-linearity (Figure 8) . Yet when the spectral energy was integrated over this frequency range and plotted as a function of AK, a systematic and abrupt increase in energy emerged (Figure 9). A slight decline in this high frequency energy was observed with the suppression of the microscale waves by the increasing swell followed by explosive growth as the mean swell steepness exceeds 0.21. This appears to be universal behaviour across all of out test regimes and may offer more general possibilities.
3. In spite of limited lighting conditions at our selected fetch in the tank, we also visually observed the wave probe location to determine the breaking probability of the swell. The limited illumination and visual access made video techniques infeasible. As best we were able, only breaking of the dominant swell were counted and breaking of microscale waves has been excluded from the statistics presented in Figure 10. We noted that when the breaking is weak, it is very difficult to make precise observations. Four 60 second ensembles of wave statistics were taken for each case and the error bars show the standard deviation of the four sets of observations.

4.2 Total Drag Measurements

The mean total stress values for each test shown as a function of the mean swell steepness in Figure 11. In each case, the stress values have been normalised in terms of the stress in the absence of the swell. The collapse of the data is remarkable.

As expected, at a mean steepness of approximately 0.25 there is a very steep transition in total drag consistent with the observations of Banner (1990). However, Banner's study was

undertaken at a short fetch in a narrower tank and the wave fields were far more uniform that we could achieve during this study. Nonetheless, each test indicates an increase in 50% of the total stress with a change in mean wave steepness from 0.21 to 0.28±0.02. It is important to note that these waves are also up to a factor of 4 longer and the mean wind forcing double of the comparable quantities used by Banner .

An unexpected result was the systematic and significant decline in total stress that occurred with the introduction of the swell. In this normalisation, the results of the four tests are indistinguishable at the degree of precision permitted by the measurements. A total stress minimum was achieved at AK=0.14±0.02 with a reduction in normalised total stress of 19±3%. All cases showed that the total stress level returned to the level observed in the absence of the swell at a swell steepness of 0.21±0.01.

Unfortunately, our original quest to examine drag behaviour at high steepnesses was frustrated as it proved impossible to generate wave fields with AK greater than 0.32 – the wave field became saturated at mean steepnesses in the vicinity of 0.28 due to dissipation of wave energy by breaking. Only the test results at 10ms^{-1} provided any slight evidence of saturation in the total stress. Further investigation of this aspect will require modulated wave fields.

Chen and Belcher (2002) have suggested that the presence of swell reduces the turbulent stress adjacent to the surface available for the growth of small wind waves. These results do not support their findings. As the mean swell steepness increases up to a value of AK=0.21, there is a systematic and corresponding reduction in the total stress. The reduction in total momentum flux suggests that a process is acting to destroy the dominant roughness element (the short wind waves). Three processes have been identified that could potentially have this effect:

1. Phillips and Banner, 1974 have proposed that the augmentation of drift prevents short waves passing the swell crest due to breaking of the short waves. They find that the energy density of the short waves falls to zero as AK approaches 0.2 – in qualitatively good agreement with these observations.
2. Donelan (1987) has proposed that disruption of the non-linear interactions between the wind waves may occur in the presence of the swell.
3. Cheung and Street (1988) show enhanced turbulent intensity beneath swell relative to wind waves alone. Coupled with the findings of Teixeira and Belcher (2002), this may preferentially disrupt the short waves.

However, once the swell has become sufficiently steep, the swell waves start to assume a dominant role in drag generation and as they cross the breaking transition, cause very rapid

increases in total drag. We now examine the data in terms of observed wind-wave drag behaviour. Due to the complexity of describing drag over the sea a number of different descriptors have been developed. We revisit these in the context of these measurements.

4.3 Parameterisations of surface drag

Roughness length

Studies of the drag response within boundary layers above solid, planar surfaces have been successful at relating velocity at a reference height to the stress via a so-called roughness length which can be related to the height of the solid, surface roughness elements. In a constant stress boundary layer, the observed velocity variation with height is logarithmic and exhibits the following form:

$$U(z)=\frac{u_*^a}{\kappa}\ln\left(\frac{z}{z_0}\right) \tag{7}$$

where z_0 is the roughness height.

$$z_0=z\,e^{-\frac{\kappa U(z)}{u_*^a}} \tag{8}$$

The development of z0 with AK (Figure 12) resembles the observed response of the stress (Figure 11). All test cases show a modest decline in the roughness length with the introduction of the swell but as the mean swell steepness exceeds 0.21, z_0 increases substantially. Note that measurement of the roughness length is difficult and our experience in the laboratory is that it is difficult to measure z0 more accurately than ±50%.

There are many normalisations of the roughness length in the literature with the most popular being: Charnock (1955) (gz_0/u_*^{a2}); non-dimensionalisation by the root-mean-square surface elevation (z_0/σ); and, drag coefficients ($C_z=(u_*^a/U_z)^2=(\kappa/\ln(z/z_0))^2$). The data normalised in these forms as a function of AK are shown in Figures 13, 14 and 15 respectively. These curves all exhibit systematic behaviour as a function of mean swell steepness as observed for normalised total drag.

Numerous methods of collapsing these normalisations have been adopted in the literature and some forms are reviewed here.

The simplest form and most popular form has to been to express the drag coefficient as a function of the wind speed at a reference level (usually 10m). The results of these

experiments are presented in the context of the data assembly of Donelan (1990) in Figure 16. It is interesting to observe that all of the data sets exhibit significant but almost singular behaviour in this normalisation. With the introduction of the swell there is a modest reduction in the drag coefficient to levels resembling those measured by Large and Pond (1981). As the swell steepness is increased, the drag coefficient also increases markedly (Figure 15) – to the extent that much of the enhancement of wave drag observed by Donelan (1990) in the laboratory and field above Large and Pond's relationship is captured. However, the observed variations in drag are almost singular in this form showing the insensitivity to the reference wind.

Donelan (1990) investigated the relationship between roughness height and root mean square surface elevation. Expressed in Reynolds number forms these are shown in Figure 17. As observed earlier both z_0 and u_*^a are modulated by the swell and consequently the roughness Reynolds number shows very strong variation in this normalisation. Approximate upper and lower bound lines for all of the data sets show a linear relationship between σ and z_0. It is interesting to note that the young wind sea data are captured within the upper and lower bound lines obtained from this study.

Many researchers have presented the roughness length as a proportion of the surface variance in terms of wave age (U_{10}/c_p) or their derivative quantities. Two representative wind speeds have been selected, consistent with Donelan (1990) and are shown in Figures 18 and 19. These normalisations have several weaknesses:

1. In multi-peaked spectra, contributions from multiple spectral components cannot be recognised. To plot our data, we have strictly used the swell phase speed in the normalisation.
2. Whilst the Donelan (1990) tank data collapses systematically, our data exhibit approximately singular behaviour and wave age is seen to be a poor predictor of normalised roughness length.

In summary, conventional non-dimensional normalisations are not successful at systematically representing the variations in total drag observed during this study. Yet, all four data sets show systematic behaviour when the total drag is normalised against a representative value and plotted as a function of the swell steepness.
Our observations can be summarised as follows:

1. Microscale breaking wind waves are able to grow rapidly and mediate intense wind-induced momentum flux.
2. However, interactions between wave scales acts to promote suppression of the smaller scale waves. The moderate levels of disruption of the microscale waves will actually lead to a slight reduction in the total drag because of this effect.

3. The development of steep, slow spectral components can generate very strong levels of drag as exhibited by the effects of the swell in this study. This suggests that waves that are steep, slow and large are primarily responsible for the very high drag coefficients that have been observed in the field. For young wind seas, these steep features may occur at the spectral peak.

Our ultimate goal is a reliable representation of total drag that will span all sea states. This study has shown that the dominant contribution to surface drag can be passed between different frequencies in the spectrum according to their contributions to the steepness of the surface.

The spectral form which locally most closely represents wave steepness information is the saturation spectrum *B(f):*

$$B(f)=S(f)f^4 \tag{9}$$

where *S*(*f*) is the conventional energy spectrum.

Donelan (1990) indicates that, in general, the tails of field and laboratory frequency spectra exhibit a constant normalised level above the spectral peak. Our spectra also approximately exhibit an approximately constant level of saturation in the gravity region of the spectral tail (Figure 20) except where the dominant microscale, swell or their harmonics dominant. These appear as local features in the saturation spectrum.

Also, it can be observed that the gravity range in the saturation spectrum also exhibits a systematic increase in saturation level with wind speed (Figure 20).

A possibility that emerges is that at any given wind speed, there is a equilibrium level of saturation in the gravity portion of the spectral tail that will be achieved due to the interactions between the different frequency components. The dominant drag waves are exhibited in the saturation spectrum by an anomaly in saturation level. By quantifying the anomaly and its speed relative to the prevailing wind, perhaps a general representative measure of sea surface roughness can be obtained.
To verify these ideas, analysis of appropriate field data sets will be necessary.

4.4 Form Drag Measurements

Static pressure measurements were obtained for the f_s=1.4Hz, U=6ms^{-1} case before premature

failure of the total tube. As discussed previously, data acquisition was undertaken without the wavemaker oscillating in order avoid wavemaker acoustic modes. Each run consisted of 5 separate time series of 22s apiece with an acquisition frequency of 300.4808 Hz. From each separate times series, a mean form drag value and a standard deviation were computed.

Figure 21 shows representative wave spectra together with the corresponding coherent and phase functions. The values obtained at the swell frequency are shown as a function of the swell steepness in Figure 22.

The form drag normalised by the total drag is presented in Figure 23. The data show an orderly an consistent development of form drag from AK=0.0 to 0.3. The error bars shown indicate the standard deviation from the measurement ensembles.

As discussed earlier, the static pressure data has not been extrapolated to the water surface so these data values underestimate the surface form drag and wind energy input. However, they sit above the curve determined by Peirson and Belcher (2004) (largely on the basis of the Bole (1967) and Bliven *et al.* (1986) measurement of actual wave growth corrected for viscous attenuation). These current measurements also sit slightly below the wave growth measurements previously obtained by Mastenbroek *et al.* (1996) from static pressure measurements in the air. An intriguing possibility is that coupled static pressure and actual wave growth measurements may be able to determine if the attenuation of wave growth by turbulence in the water is an important process. Also, using similar techniques the wave energy loss of wind-forced, actively breaking waves could also be determined across a range of wave scales.

5. CONCLUSIONS AND RECOMMENDATIONS

The findings of this study are as follows:

1. The introduction of lower frequency waves beneath microscale waves disrupts the microscale in such a way that the total stress borne by the surface can fall by approximately 20%. For the narrow-banded spectra used during this study, this decline in total stress is systematic in terms of the low frequency wave steepness.
2. Once the low frequency waves achieve a steepness greater than approximately 0.15, their presence starts to augment the stress which then rises rapidly after they achieve a mean steepness of 0.20.
3. Consistent behaviour was observed when the total stress was normalised by the stress in the absence of the paddle waves.
4. The enhancement of the stress was observed to be concomitant with changes in spectral energy in the frequency range 8 to 30 Hz. We do not believe that the steep rise in drag is due to this high frequency activity. Rather, both are a reflection of the aerodynamic and hydrodynamic effects associated with steep waves assuming an actively breaking condition.
5. Limited form drag measurements obtained during this study show consistent development of form drag with mean wave steepness that has not previously been observed. In comparison with the results of Bliven *et al.* (1986), these results may provide preliminary evidence of partial suppression of wave growth by turbulence.

Parameterising drag over the open ocean has remained a difficult and unfulfilled task. However, our current findings prompt the following tentative predictions regarding drag over the deep ocean:

1. Microscale breaking wind waves are able to grow rapidly and mediate intense wind-induced momentum flux. In the absence of lower frequency waves (laboratory tanks, gusts), microscale waves will form and mediate intense levels of drag.
2. Interactions between wave scales acts to promote suppression of the smaller scale waves. For very old wind seas with low mean slopes at the spectral peak, the tail also becomes saturated with modest levels of mean steepness. Under such conditions, the total drag becomes less than would be observed in conventional laboratory wind tanks at equivalent U_{10} due to the disruption of the slow waves.
3. Steep, slow spectral components can generate very strong levels of drag and it is these components that are primarily responsible for the very high drag coefficients that have been observed in the field. For young wind seas, these steep features may occur at the spectral peak.
4. Obtaining better estimates of total drag over the sea requires focus on the tail of the spectrum – specifically, the saturation spectrum needs to be scanned for spectral

components exceeding a specified level and relationships developed between the anomaly in the saturation spectrum and the observed enhancement of the stress.

The success of this investigation indicates that the following studies should provide incisive insights into wind-forced wave behaviour:

1. A review of appropriate field data sets to determine a relationship between anomalies in the saturation spectrum and enhanced drag. This would extend the findings of this study to field operational application.
2. A more extensive programme of laboratory measurements of the wind-induced form drag possibly coupled with concomitant measurements of wave field development. These offer the prospect of: a. being the first reliable tests of the radiation balance equation; b. directly determining the breaking losses of metre-scale, wind-forced waves; and, determining the potential role for wave-turbulence interactions in the development of wind seas.
3. Laboratory measurements of total drag over broader steep spectra at longer fetch. These could extend the findings of this study to unsteady wind and wave fields.
4. More extensive investigation of the implications of the strong enhancement of gravity-capillary activity observed in the presence of steep gravity waves for remote sensing of the ocean surface.

6. ACKNOWLEDGEMENTS

This study was only possible with the support of three educational groups.

The CNRS and the Universités d'Aix-Marseille I et II provided facilities and staff time at their Institut de Recherche sur les Phénomènes Hors Equilibre where the investigations were undertaken.

The University of New South Wales provided financial support for Dr. Peirson whilst on study leave and a faculty research grant for the purpose of undertaking this investigation.

The Ecole des Mines d'Alès very kindly hosted Dr. Peirson during his study leave and provided hospitality for Dr. Branger during the later stages of the investigation.

The investigators would like to thank specifically Messieurs Bertrand Zucchini and Alain Laurence for their very helpful and careful technical assistance during the study.

7. REFERENCES

Banner, M.L. (1990) The influence of wave breaking on the surface pressure distribution in wind-wave interactions. *J. Fluid. Mech.* **211**, pp 463-495

Banner, M.L. and Melville, W.K. (1976) On the separation of air flow above water waves. *J. Fluid. Mech.* **77**, pp 825-842

Belcher, S.E., and Hunt, J.C.R., (1998) Turbulent flow over hills and waves. *Ann. Rev. Fluid. Mech.* **30**, 507-538

Benjamin T.B., Feir J.E., (1967), The disintegration of wave trains on deep water, *J. Fluid. Mech.*, **27**, 417-430

Bliven, L.F., Hwang, N.E. and Long, S.R. (1986) Experimental study of the influence of wind on Benjamin-Feir sideband instability. *J. Fluid Mech.* **162**, 237-260

Bole, J.B. (1967) *Response of gravity water waves to wind excitation.* Ph.D. thesis. Dept. of Civil Engineering. Stanford University.

Chanson, H. (1994) Hydraulic design of stepped cascades, channels, weirs and spillways. Pergamon.

Charnock, H. (1955) Wind stress on a water surface. *Quart. J. Roy. Met. Soc.*, **81**, 639-640.

Cheung, TK und Street, RL, 1988 The turbulent layer in the water at an air-water interface, *J. Fluid Mech.* , **194**, pp. 133-151

Donelan, MA 1987. The Effect of Swell on the Growth of Wind Waves. Johns Hopkins APL Tech. Digest 8, 18-23

Donelan, M.A. (1990) Air-Sea Interaction. in *The Sea: Ocean Engineering Science.* Vol. 9 *pp* 239-292. Wiley

Donelan, M.A., Dobson, F.W., Smith, S.D. and Anderson, R.J. (1993) The Dependence Of Sea-Surface Roughness On Wave Development. *J. Phys. Oceanog* **23**: 2143-2149

Giovanangeli, J. P. and P. Chambaud, 1987. Pressure, velocity, and temperature sensitivities of a bleed-type pressure sensor. *Review of Scientific Instruments* Vol **58**(7) pp. 1221-1225. July 1987

Hasselmann, S., Bennefield, C. et al. (1998) *Intercomparison of two-dimensional wave spectra obtained from microwave instruments, buoys and WAModel simulations during the Surface Wave Dynamics Experiment.* Max Planck Institute for Meteorology Report 258, ISSN 0937-1060.

Jones ISF, Toba Y (1995) The Dependence Of Sea-Surface Roughness On Wave Development – Comment. *J. Phys. Oceanog* **25** (8): 1905-1907 AUG 1995

Kharif Ch. And Ramamonjiarisoa A., (1988), Deep water gravity wave instabilities et large steepness, *Phys. Fluid*, **31**, 5, 1286-1288

Large, W.G. and Pond, S. (1981) Open Ocean momentum flux measurement in moderate to strong winds. *J. Phys. Oceanogr.,* **11**, 324-336.

Makin, V.K. and Kudryavtsev, V.N. (2002) Impact of Dominant Waves on Sea Drag.

Boundary Layer Met., **103**: 83-99.

Mastenbroek, C., Makin, V.K., Garat, M.H. and Giovanangeli, J.P. (1996) Experimental evidence of the rapid distortion of turbulence in the air flow over water waves. *J. Fluid Mech.* , **318**, 273-302

Melville, W.K. 1982 Instability and breaking of deep-water waves. *J. Fluid Mech.* **115**, 165-185.

Mitsuyasu, H. (1966) Interactions between water waves and wind (I). *Rep. Res. Inst. Appl. Mech. , Kyushu University*, **14**, 67-88.

Peirson, W.L., Garcia, A.W. and Pells, S.E. 2003 Water-Wave Attenuation Due To Opposing Wind. *J. Fluid Mech.* . **487**, 345-365.

Peirson, W.L. and Belcher, S.E. (2004) On the relationship between the energy and momentum fluxes from wind to slow water waves. Submitted for review to the *J. Fluid Mech.*

Phillips, O.M. and Banner, M.L. (1974) Wave breaking in the presence of wind drift and swell. *J. Fluid Mech.*, **66**. Part 4. 625-640

Powell, M.D., Vickery, P.J. and Reinhold, T.A., (2003) Reduced drag coefficient for high wind speeds in tropical cyclones. *Nature*, **422**, 20 March.

Reul, N., Branger, H. and Giovanangeli, J-P. (1999) Air flow separation over unsteady breaking waves. *Phys. Fluids.*, **11**, No. 7. July.

Teixeira, M.A. and Belcher, S.E. (2002) On the distortion of turbulence by a progressive surface wave. *J. Fluid Mech.*, **458**, 229-267

Wright, C.W., E.J. Walsh, D. Vandemark, W.B. Krabill, A.W. Garcia, S.H. Houston, M.D. Powell, P.G. Black, and F.D. Marks (2001) Hurricane directional wave spectrum spatial variation in the open ocean, *J. Phys. Ocean.*, **31**, 2472-2488

8. APPENDIX A: TABULATED RESULTS

Table 2. Summary Results for f_p=2.0Hz, U=6.0m/s

	u* (m/s)	AK	z (m)	U(z) (m/s)	z0 (m)	U_{10} (m/s)	H1/3 (cm)	sigma (cm)	Hmax (cm)	var(AK)
C000060B	0.254	0.000	0.0750	4.58	0.00005529	7.69	2.15	0.57	3.43	0.0185
C000060A	0.261	0.000	0.0750	4.57	0.00006813	7.76	2.22	0.56	3.35	0.0180
E000060A	0.252	0.000	0.0710	4.14	0.00009939	7.26	1.89	0.53	3.25	0.0168
E000060B	0.257	0.000	0.0710	4.21	0.00010128	7.39	2.02	0.54	3.41	0.0164
E201060A	0.236	0.097	0.0710	4.31	0.00004772	7.23	1.83	0.49	3.13	0.0114
E201060B	0.238	0.094	0.0710	4.3	0.00005160	7.24	1.64	0.43	2.72	0.0098
C202060A	0.220	0.150	0.0750	4.63	0.00001656	7.32	2.52	0.7	3.13	0.0134
C202060B	0.229	0.145	0.0750	4.53	0.00002746	7.33	2.37	0.65	3.18	0.0127
C203060A	0.228	0.152	0.0750	4.65	0.00002148	7.44	2.5	0.69	3.44	0.0131
C203060B	0.221	0.131	0.0750	4.7	0.00001516	7.4	1.96	0.52	2.9	0.0102
C204060A	0.253	0.209	0.0750	4.62	0.00005045	7.71	3.3	0.95	4.68	0.0226
C204560A	0.249	0.206	0.0750	4.67	0.00004140	7.72	3.44	0.91	4.36	0.0213
C204560B	0.269	0.220	0.0750	4.61	0.00007906	7.9	3.47	0.96	4.29	0.0239
E204560A	0.262	0.182	0.0710	4.3	0.00010004	7.54	2.97	0.76	4.35	0.0160
E204560B	0.260	0.217	0.0710	4.29	0.00009659	7.51	3.53	1	4.73	0.0249
C205060A	0.301	0.264	0.0750	4.49	0.00019219	8.17	4.59	1.31	6.03	0.0354
C205060B	0.289	0.220	0.0750	4.51	0.00014592	8.05	3.71	1.01	5.11	0.0242
C205060C	0.287	0.221	0.0750	4.56	0.00013030	8.07	3.63	1.01	5.08	0.0247
E205060A	0.302	0.243	0.0710	4.16	0.00028729	7.9	4.16	1.14	5.47	0.0298
E205060B	0.291	0.241	0.0710	4.18	0.00022695	7.78	3.8	1.09	4.97	0.0296

Table 3. Summary Results for f_p=1.6Hz, U=8.0m/s

	u* (m/s)	AK	z (m)	U(z) (m/s)	z0 (m)	U_{10} (m/s)	H1/3 (cm)	sigma (cm)	Hmax (cm)	var(AK)
H000080A	0.37	0	0.0438	5.46	0.00012352	10.51	3	0.86	4.9904	0.0261
H000080B	0.38	0	0.0438	5.41	0.00014080	10.53	3.09	0.82	4.6352	0.0247
H160580A	0.37	0.02	0.0435	5.37	0.00012294	10.35	2.87	0.73	4.3541	0.0197
H160580B	0.37	0.02	0.0435	5.29	0.00014063	10.31	2.86	0.73	4.3541	0.0197
H160880A	0.35	0.03	0.0435	5.4	0.00009408	10.19	2.64	0.73	4.7894	0.0198
H160880B	0.35	0.05	0.0435	5.4	0.00009740	10.21	2.7	0.73	4.7894	0.0198
H161080A	0.35	0.08	0.0438	5.57	0.00007809	10.35	2.36	0.65	3.7961	0.0154
H161080B	0.36	0.1	0.0438	5.55	0.00009034	10.42	2.72	0.74	4.9334	0.0164
H162080A	0.35	0.13	0.0438	5.68	0.00006045	10.36	2.89	0.79	4.7702	0.0140
H162080B	0.34	0.11	0.0438	5.72	0.00005553	10.38	2.7	0.74	4.2124	0.0133
H163080A	0.35	0.15	0.0503	5.82	0.00006136	10.41	3.62	1.01	4.8547	0.0153
H163080B	0.35	0.17	0.0503	5.81	0.00006827	10.47	3.95	1.07	5.5233	0.0168
H164080A	0.38	0.22	0.0633	5.84	0.00013541	10.65	5.31	1.57	6.4495	0.0271
H164080B	0.36	0.19	0.0633	5.88	0.00009039	10.42	4.77	1.32	6.5732	0.0210
H165080A	0.38	0.22	0.0658	5.87	0.00014544	10.69	5.79	1.58	7.5933	0.0278
H165080B	0.38	0.27	0.0658	5.92	0.00013586	10.73	6.42	1.91	8.2168	0.0383
H166080A	0.45	0.3	0.0813	5.66	0.00050183	11.01	7.53	2.14	9.5167	0.0456
H166080B	0.42	0.27	0.0813	5.67	0.00034862	10.67	6.96	1.92	8.6235	0.0377
H167080A	0.46	0.3	0.0946	5.51	0.00076907	10.85	8.02	2.23	10.0572	0.0484
H167080B	0.46	0.32	0.0946	5.58	0.00075464	10.96	8.62	2.39	10.6041	0.0536
H168080A	0.46	0.29	0.0946	5.51	0.00074505	10.81	7.76	2.17	10.2258	0.0436
H168080B	0.44	0.3	0.0946	5.54	0.00061465	10.67	7.79	2.18	10.6417	0.0448
H169980A	0.41	0.28	0.0899	5.5	0.00042014	10.33	7.78	2.05	10.1944	0.0401
H169980B	0.43	0.29	0.0899	5.52	0.00052931	10.59	8.19	2.15	11.2544	0.0427

Table 4. Summary results with f_p=1.4Hz, U=6m/s

	u* (m/s)	AK	z (m)	U(z) (m/s)	z0 (m)	U_{10} (m/s)	H1/3 (cm)	sigma (cm)	Hmax (cm)	var(AK)
I000060A	0.262	0.000	0.0623	3.84	0.0001772	7.166	2.240	0.565	3.7934	0.0176
I000060B	0.272	0.000	0.0626	3.90	0.0002022	7.350	2.190	0.574	3.3075	0.0183
I140560A	0.257	0.008	0.0480	3.68	0.0001562	7.110	2.220	0.558	3.6131	0.0181
I140560B	0.261	0.012	0.0480	3.66	0.0001759	7.144	2.240	0.568	3.6131	0.0181
I140860A	0.257	0.028	0.0480	3.70	0.0001514	7.130	2.220	0.597	3.4720	0.0170
I140860B	0.259	0.030	0.0480	3.80	0.0001357	7.257	2.100	0.540	3.4720	0.0170
I141060A	0.263	0.042	0.0626	3.94	0.0001564	7.276	2.140	0.547	3.5661	0.0153
I141060B	0.261	0.040	0.0626	3.98	0.0001405	7.291	2.310	0.589	3.4681	0.0180
I142060A	0.243	0.087	0.0626	4.16	0.0000665	7.242	2.660	0.707	3.8953	0.0140
I142060B	0.250	0.093	0.0626	4.16	0.0000805	7.331	2.970	0.789	4.0285	0.0150
I143060A	0.248	0.099	0.0677	4.20	0.0000774	7.297	2.980	0.799	4.0834	0.0141
I143060B	0.240	0.109	0.0677	4.16	0.0000660	7.157	3.530	0.940	4.3499	0.0141
I144060A	0.258	0.122	0.0726	4.26	0.0000983	7.437	3.800	1.032	4.5615	0.0153
I144060B	0.243	0.144	0.0726	4.27	0.0000643	7.262	4.290	1.249	5.2316	0.0165
I144560A	0.254	0.175	0.0888	4.19	0.0001210	7.190	5.190	1.640	5.9174	0.0194
I144560B	0.249	0.163	0.0888	4.26	0.0000947	7.201	4.790	1.497	5.5373	0.0181
I144860A	0.250	0.189	0.0888	4.36	0.0000829	7.312	5.680	1.763	6.5522	0.0223
I144860B	0.240	0.191	0.0888	4.36	0.0000620	7.194	5.880	1.792	6.7599	0.0226
I145060A	0.245	0.183	0.0849	4.32	0.0000734	7.241	5.370	1.694	6.0232	0.0205
I145060B	0.241	0.177	0.0849	4.33	0.0000642	7.203	5.140	1.597	5.7920	0.0196
I146060A	0.268	0.207	0.0885	4.35	0.0001341	7.517	6.290	1.998	7.2889	0.0248
I146060B	0.265	0.218	0.0885	4.33	0.0001284	7.462	6.640	2.123	7.1322	0.0266
I147060A	0.282	0.238	0.0935	4.32	0.0002040	7.614	7.350	2.336	8.6017	0.0317
I147060B	0.282	0.247	0.0935	4.31	0.0002069	7.604	7.620	2.448	8.6057	0.0337
I148060A	0.287	0.271	0.0982	4.26	0.0002592	7.577	8.140	2.582	9.5618	0.0396
I148060B	0.284	0.269	0.0982	4.18	0.0002724	7.463	8.150	2.580	9.0994	0.0387
I149060A	0.308	0.289	0.1043	4.28	0.0004021	7.794	9.170	2.773	10.0086	0.0455
I149060B	0.317	0.297	0.1043	4.21	0.0005143	7.826	9.210	2.840	10.3691	0.0474
I149960A	0.335	0.315	0.1130	4.13	0.0008155	7.884	10.090	3.069	11.5643	0.0537
I149960B	0.333	0.303	0.1130	4.13	0.0007917	7.862	9.690	2.928	11.0196	0.0506

Table 5. Summary results with f_p=1.4Hz, U=10m/s

	u* (m/s)	AK	z (m)	U(z) (m/s)	U_{10} (m/s)	H1/3 (cm)	sigma (cm)	Hmax (cm)	var(AK)	sigma (m)
G000010A	0.5	0	0.0690	7.1	13.36	4.01	1.05	5.95	0.03	0.01047
G000010B	0.51	0	0.0690	7.18	13.52	4.04	1.07	6.32	0.03	0.01069
G140510A	0.49	0.03	0.0651	7.06	13.21	3.87	1.06	6.49	0.03	0.01059
G140510B	0.49	0.02	0.0710	7.06	13.13		1.05	6.77	0.03	0.01053
G140810A	0.48	0.09	0.0651	7.16	13.16	5.79	1.01	5.96	0.02	0.01012
G140810B	0.48	0.04	0.0651	7.13	13.12	5.86	0.95	5.99	0.02	0.00948
G141010A	0.47	0.12	0.0730	7.45	13.17	4.3	1.18	6.23	0.02	0.01184
G141010B	0.48	0.11	0.0730	7.35	13.2	3.91	1.04	6.18	0.02	0.01039
G142010A	0.47	0.12	0.0726	7.46	13.26	3.9	1.08	6.94	0.02	0.01082
G142010B	0.46	0.1	0.0726	7.37	12.97	3.34	0.95	5.74	0.02	0.00945
G143010A	0.47	0.13	0.0777	7.55	13.2	4.51	1.28	6.23	0.02	0.01277
G143010B	0.46	0.15	0.0777	7.59	13.21	5.3	1.45	7.78	0.02	0.01446
G144010A	0.47	0.17	0.0759	7.42	13.16	5.84	1.73	8.07	0.02	0.01735
G144010B	0.49	0.19	0.0759	7.35	13.35	6.32	1.93	7.81	0.02	0.01927
G144510A	0.5	0.22	0.1014	7.83	13.55	7.58	2.21	9.57	0.03	0.02215
G144510B	0.47	0.2	0.1014	7.85	13.29	6.86	2.02	8.44	0.03	0.02017
G144810A	0.5	0.26	0.1151	7.83	13.43	8.29	2.54	9.9	0.04	0.02535
G144810B	0.5	0.25	0.1151	7.8	13.4	8.46	2.49	10.33	0.04	0.02491
G145010A	0.56	0.27	0.1108	7.7	14.03	8.54	2.64	10.09	0.04	0.02643
G146010A	0.65	0.32	0.1205	7.25	14.44	10.68	3.22	13.44	0.06	0.03225
G146010B	0.66	0.32	0.1205	7.26	14.51	10.69	3.21	12.79	0.06	0.03208
G147010A	0.66	0.28	0.1320	7.25	14.4	10.02	2.82	12.59	0.05	0.02818
G147010B	0.69	0.28	0.1320	7.18	14.6	9.78	2.88	12.31	0.05	0.02881
G148010A	0.6	0.27	0.1317	7.26	13.78	9.27	2.6	12.53	0.04	0.02600
G148010B	0.62	0.27	0.1317	7.24	13.97	9.16	2.61	12.26	0.04	0.02612
G149010A	0.63	0.26	0.1306	7.22	14.01	9.19	2.53	12.08	0.04	0.02534
G149010B	0.62	0.28	0.1306	7.16	13.88	9.73	2.8	13.26	0.04	0.02803
G149910A	0.62	0.26	0.1328	7.23	13.94	9.22	2.54	13.02	0.04	0.02536
G149910B	0.6	0.26	0.1328	7.17	13.67	8.97	2.48	12.32	0.04	0.02484

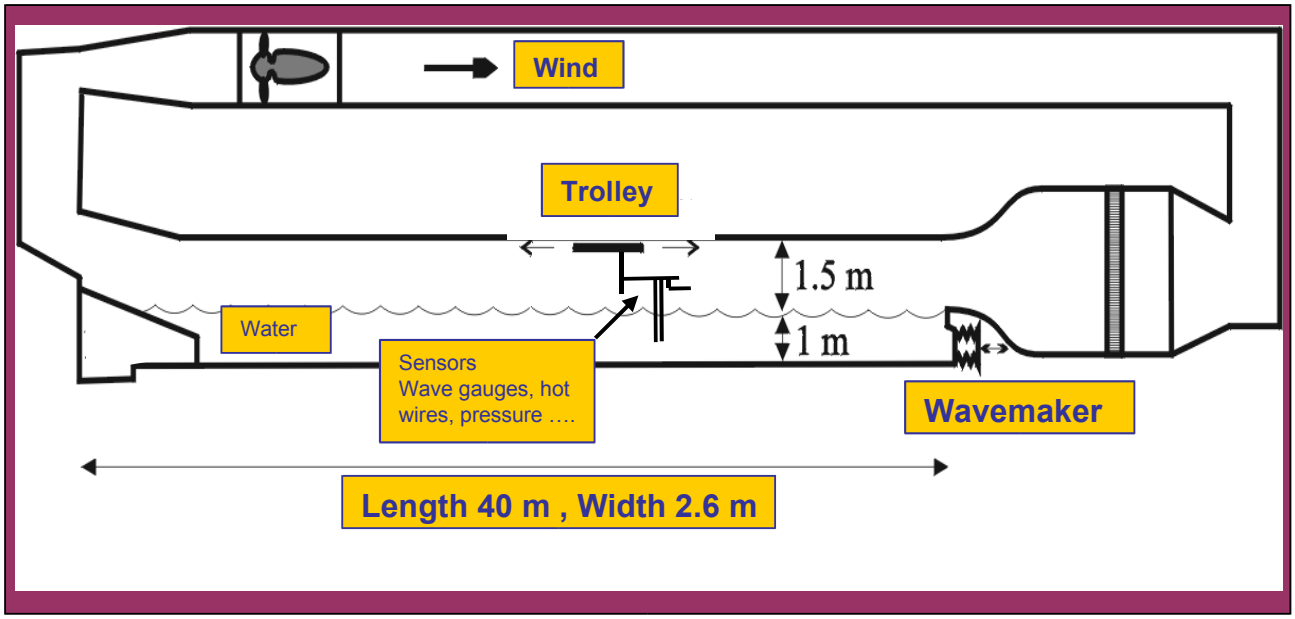

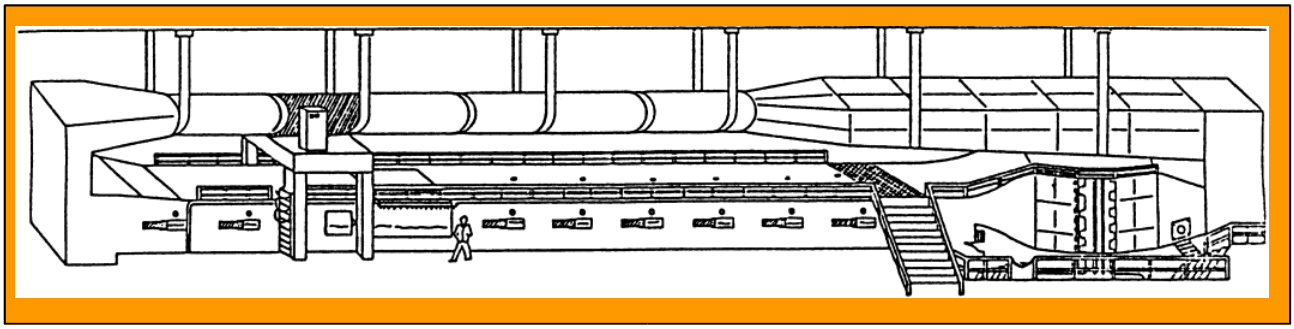

WRL Report No. 223	TANK CONFIGURATION	Figure 1 Figures050217.sxw

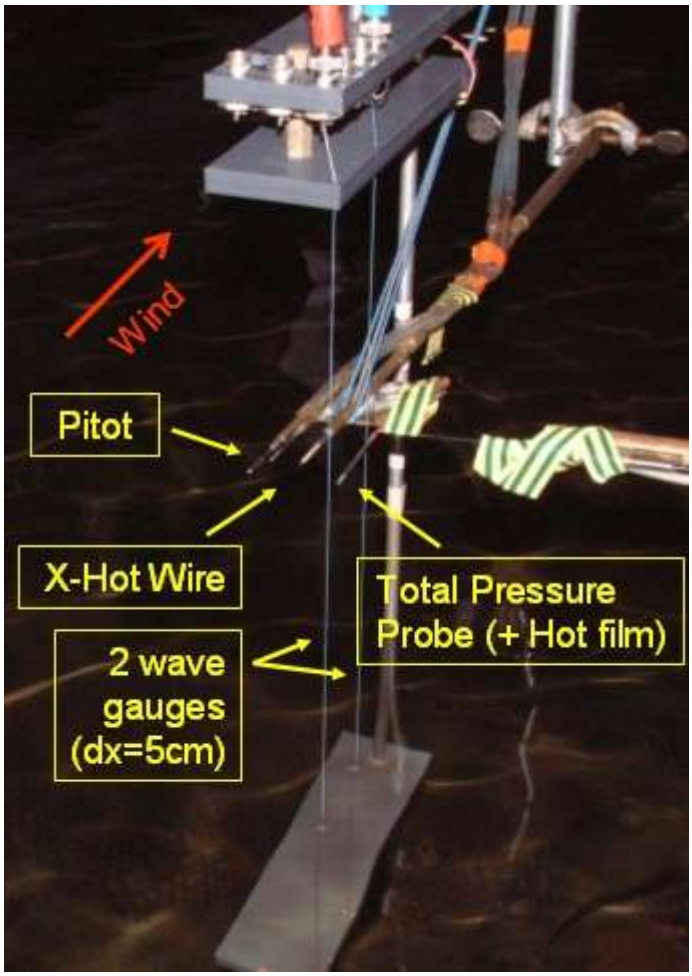

WRL Report No. 223	LAYOUT OF WAVE PROBE ARRAY	Figure 2
		Figures050217.sxw

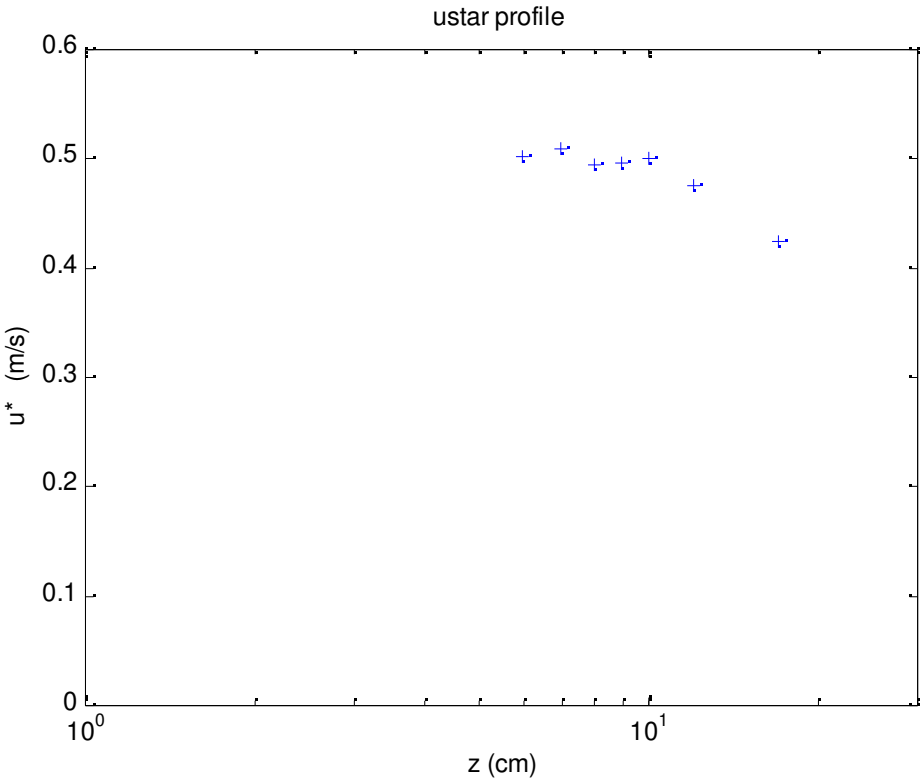

WRL Report No. 223	MEASUREMENTS OF FRICTION VELOCITY AT A WIND SPEED OF 10m/s AND SHOWING A CONSTANT STRESS LAYER BELOW 100mm ELEVATION	Figure 3 Figures050217.sxw

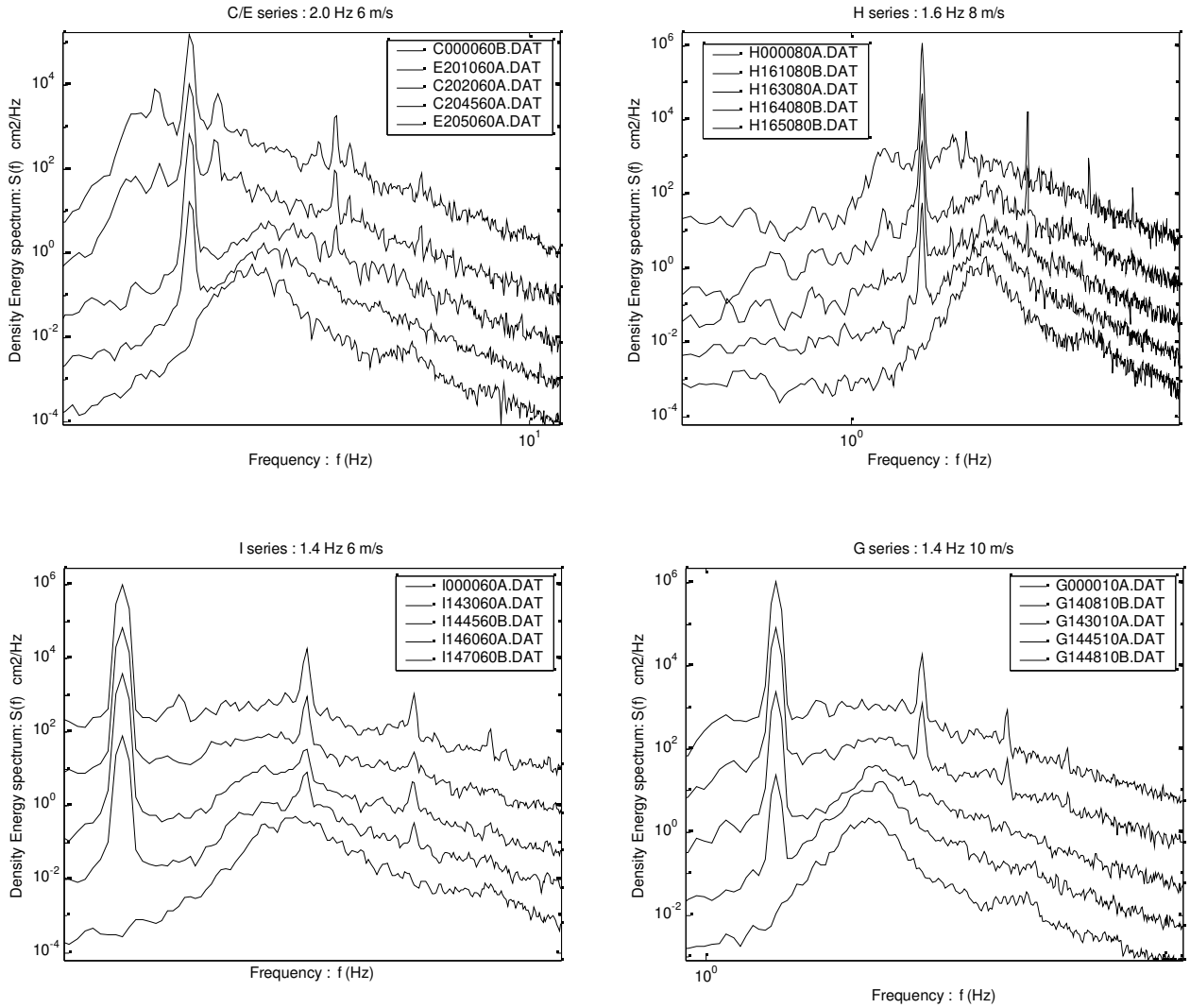

Each panel shows spectra for representative mean swell steepnesses of AK=0.00, 0.10, 0.15, 0.20 and 0.25 stacked increasing in one decade increments. Top left: U=6ms^{-1}, f_s=2.0Hz. Top right: U=8ms^{-1}, f_s=1.6Hz. Lower left : U=6ms^{-1}, f_s=1.4Hz. Lower right: U=10ms^{-1}, f_s=1.4Hz.

WRL Report No. 223	STACKED REPRESENTATIVE WAVE SPECTRA	Figure 4 Figures050217.sxw

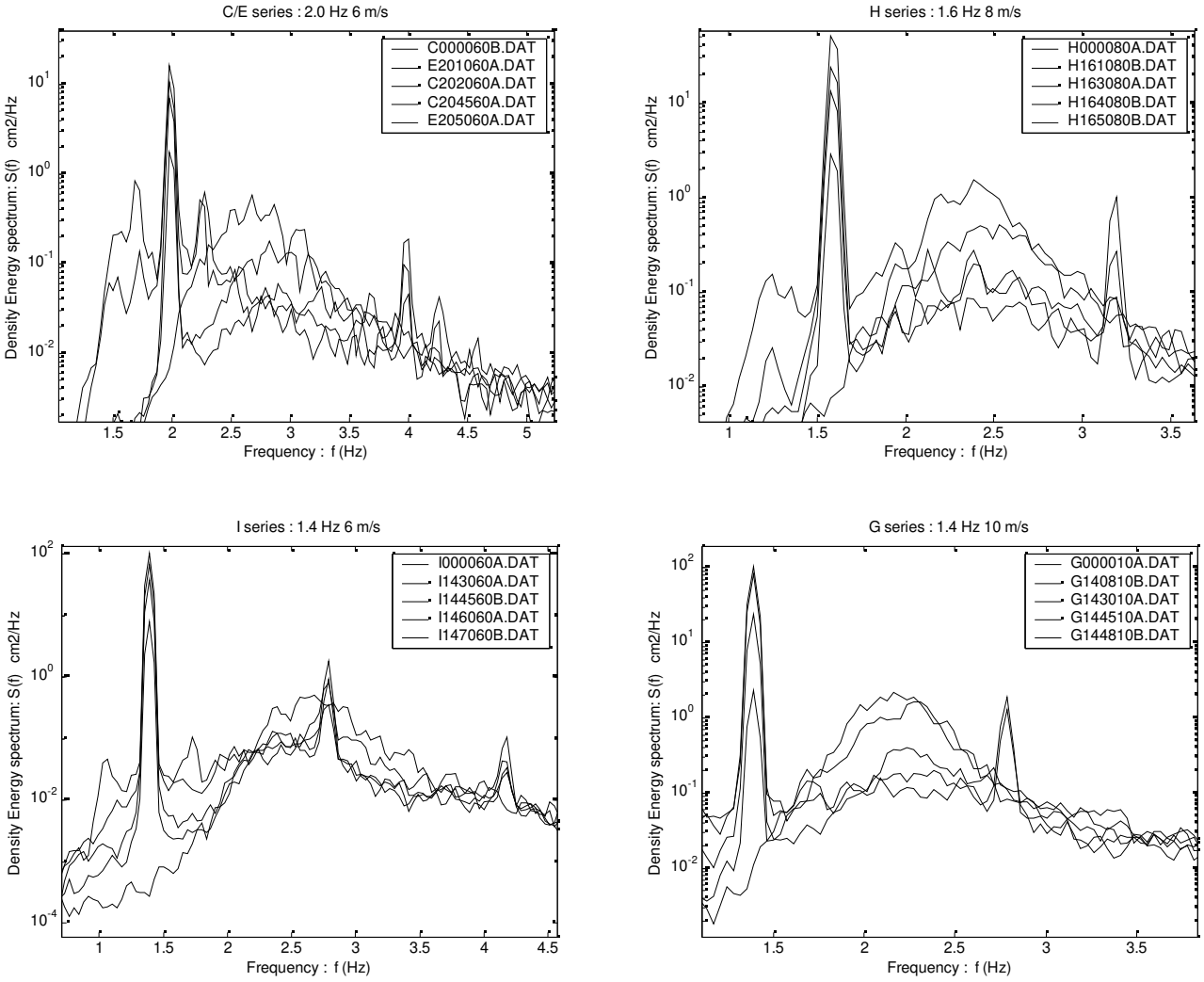

Each panel shows spectra for representative mean swell steepnesses of AK=0.00 , 0.10, 0.15 , 0.20 and 0.25 line styles in legend show are increasing AK from top to bottom.
Top left panel: U=6ms^{-1}, f_s=2.0Hz. Top right: U=8ms^{-1}, f_s=1.6Hz. Lower left : U=6ms^{-1}, f_s=1.4Hz. Lower right: U=10ms^{-1}, f_s=1.4Hz.

WRL Report No. 223	REPRESENTATIVE WAVE SPECTRA	Figure 5 Figures050217.sxw

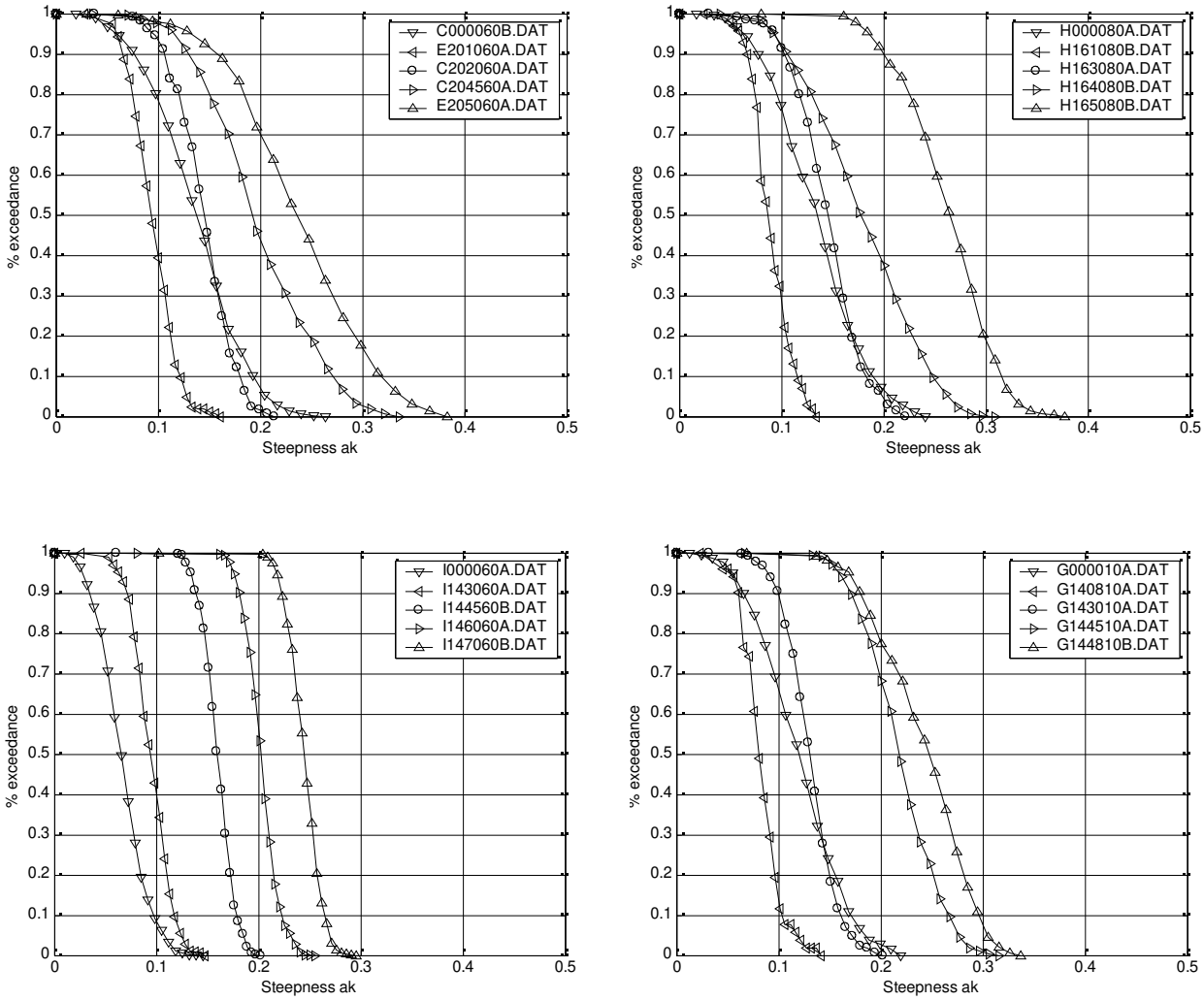

Each panel shows distributions for representative mean swell steepnesses of AK=0.00 (triangles down), 0.10(triangles left), 0.15 (circles), 0.20 (triangles right) and 0.25 (triangles up) .
Top left panel: U=6ms^{-1}, f_s=2.0Hz. Top right: U=8ms^{-1}, f_s=1.6Hz. Lower left : U=6ms^{-1}, f_s=1.4Hz. Lower right: U=10ms^{-1}, f_s=1.4Hz.

WRL Report No. 223	EXCEEDANCE DISTRIBUTIONS OF LOCAL WAVE MEAN STEEPNESS	Figure 6 Figures050217.sxw

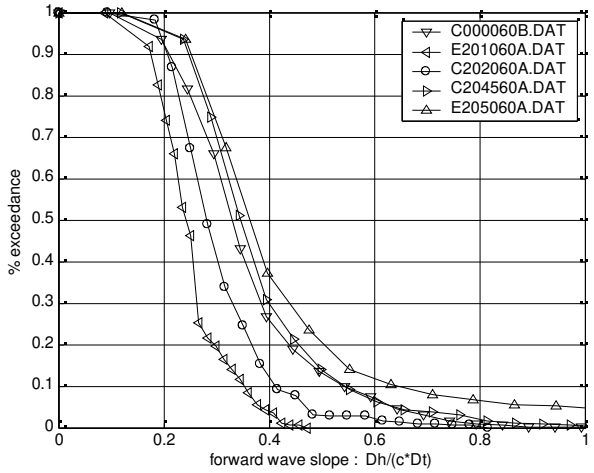

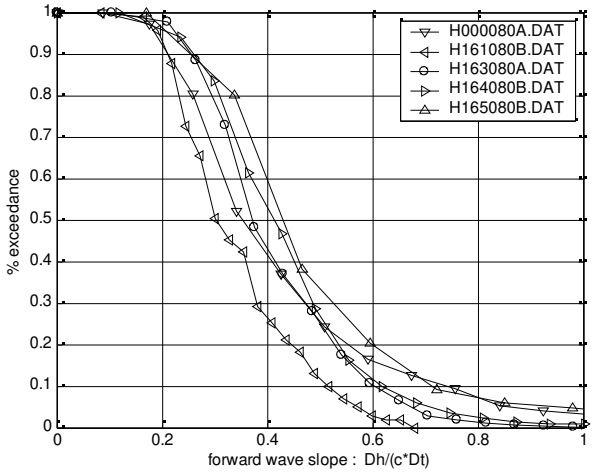

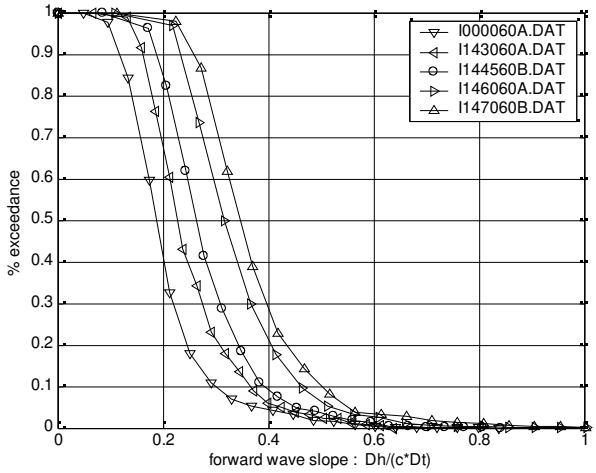

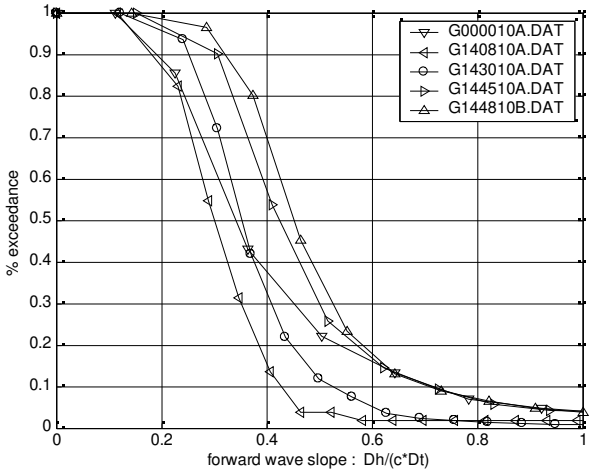

Each panel shows distributions for representative mean swell steepnesses of AK=0.00 (triangles down), 0.10(triangles left), 0.15 (circles), 0.20 (triangles right) and 0.25 (triangles up).

Top left panel: U=6ms^{-1}, f_s=2.0Hz. Top right: U=8ms^{-1}, f_s=1.6Hz. Lower left : U=6ms^{-1}, f_s=1.4Hz. Lower right: U=10ms^{-1}, f_s=1.4Hz.

WRL Report No. 223	EXCEEDANCE DISTRIBUTIONS OF LOCAL WAVE MAXIMUM STEEPNESS	Figure 7 Figures050217.sxw

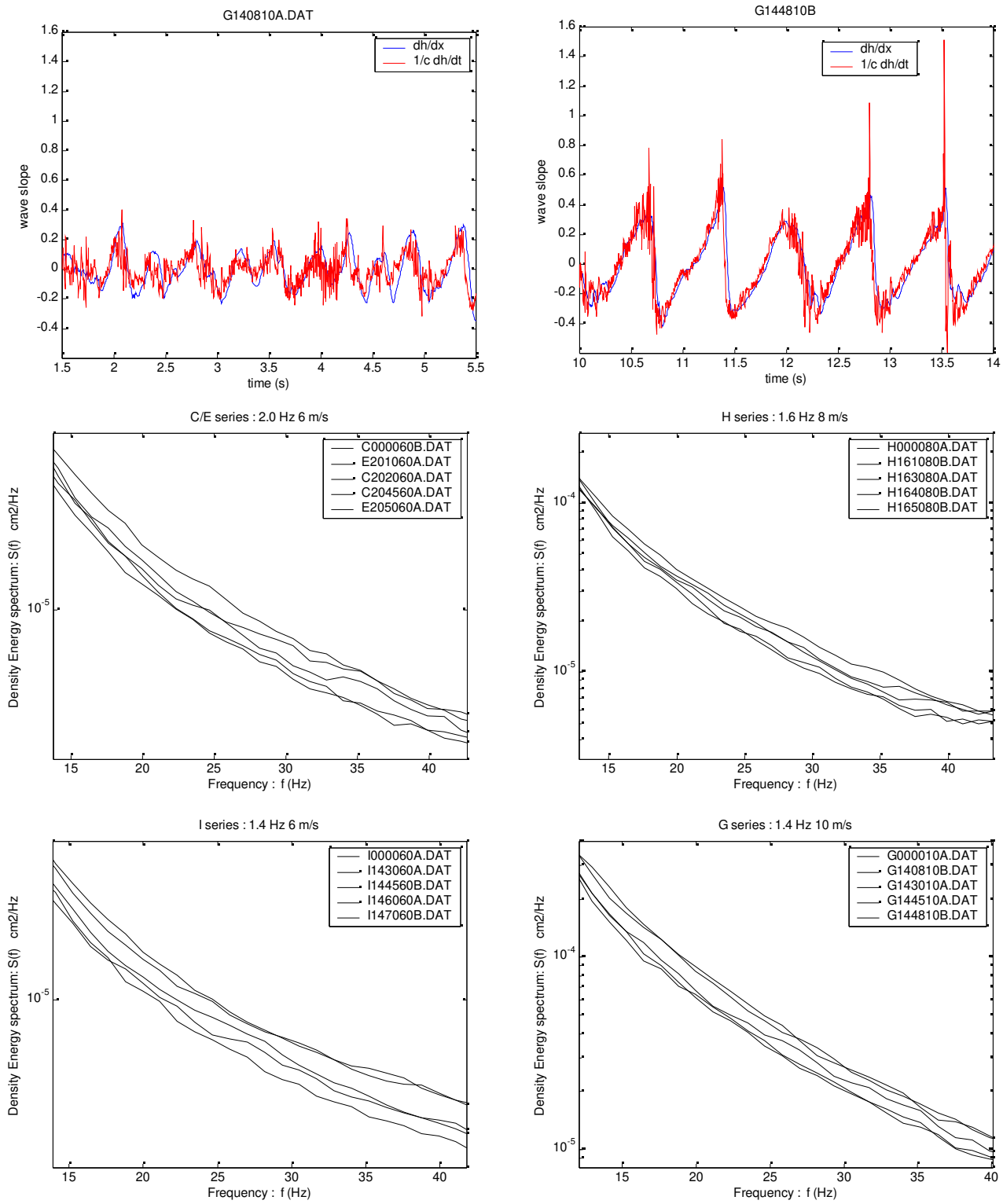

Top left: A representative surface elevation record showing limited high frequency (8-30Hz) energy in the presence of a low steepness wave train. The blue line indicates slope computed by differencing water levels at the two gauges, the red line is the computed slope from the wave speed multiplied by the time rate of change of water level. Top right: Similar to the top right panel but a steep wave train with active breaking waves. Middle left: Spectral detail between 15 and 40Hz showing development of spectral energy for representative mean wave steepnesses of AK=0.0, 0.1, 0.15, 0.2 and 0.25, U=6ms^{-1}, f_s=2.0Hz. Middle right: same as for middle left but with U=8ms^{-1}, f_s=1.6Hz. Lower left : same as for middle left but with U=6ms^{-1}, f_s=1.4Hz. Lower right: same as for middle left but with U=10ms^{-1}, f_s=1.4Hz.

WRL Report No. 223	SPECTRAL ENERGY BETWEEN 8 AND 30Hz	Figure 8 Figures050217.sxw

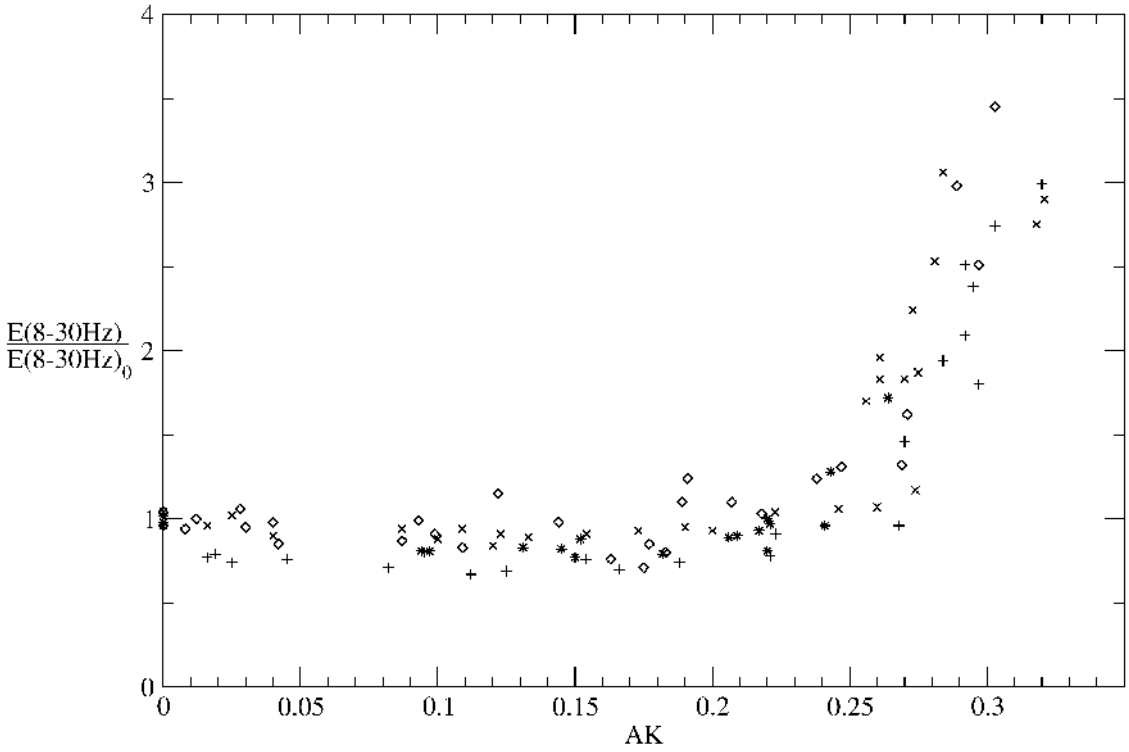

WRL Report No. 223	DEVELOPMENT OF ENERGY BETWEEN 8 AND 30Hz AS A FUNCTION OF MEAN SWELL STEEPNESS	Figure 9 Figures050217.sxw

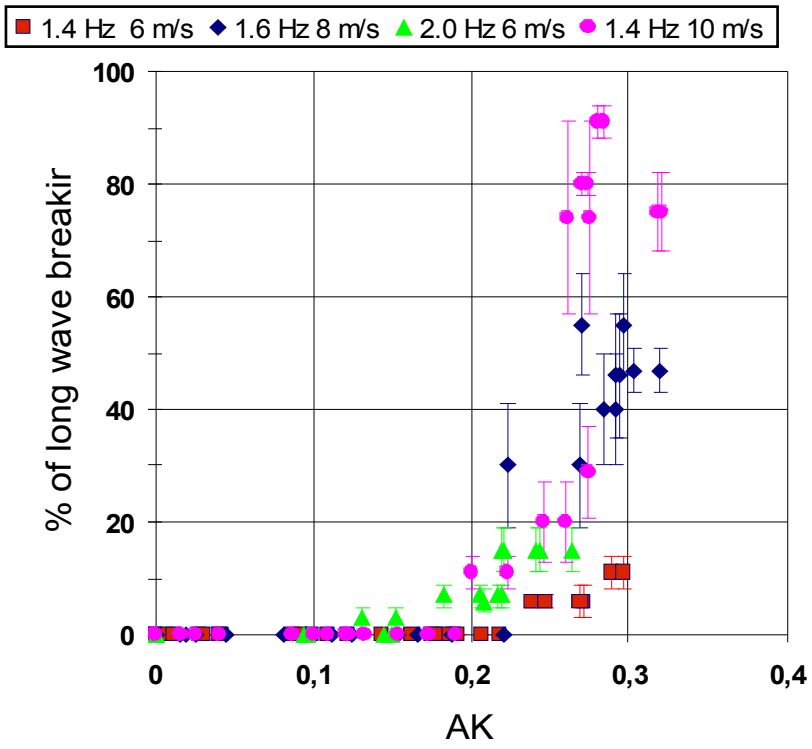

Note: error bars indicated the standard deviation derived from four 60s sample observations at each data point.

WRL Report No. 223	Swell breaking statistics obtained by visual observation.	Figure 10 Figures050217.sxw

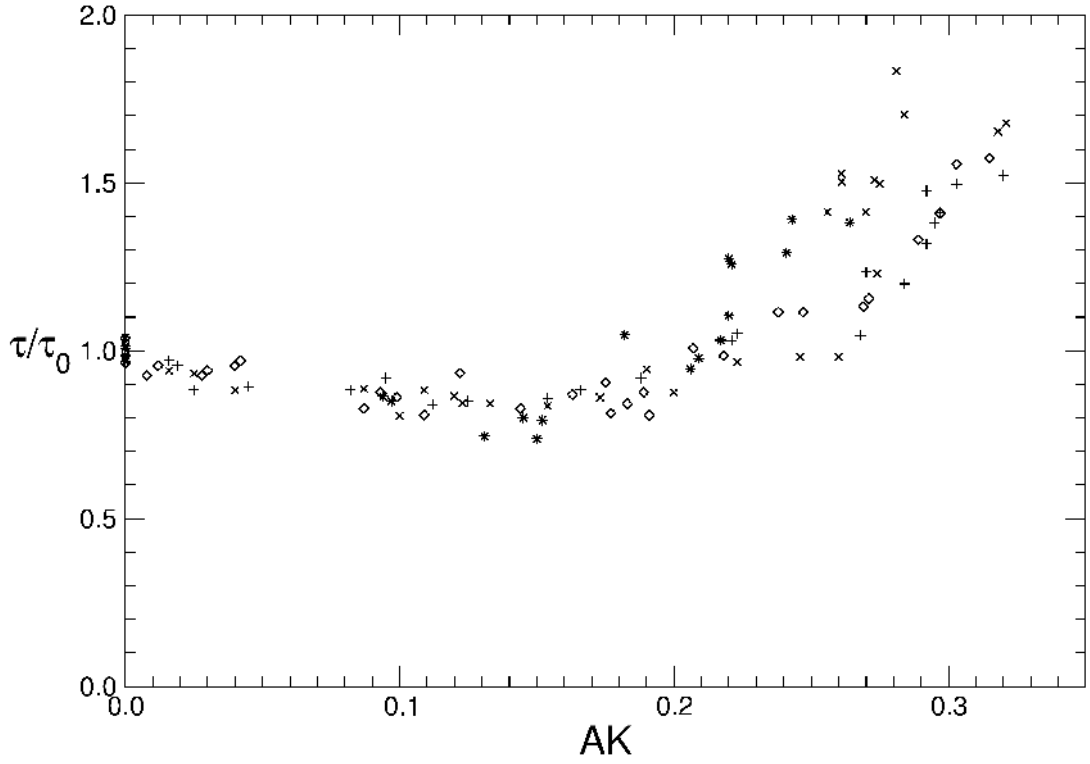

WRL Report No. 223	NORMALISED STRESS AS A FUNCTION OF AK	Figure 11 Figures050217.sxw

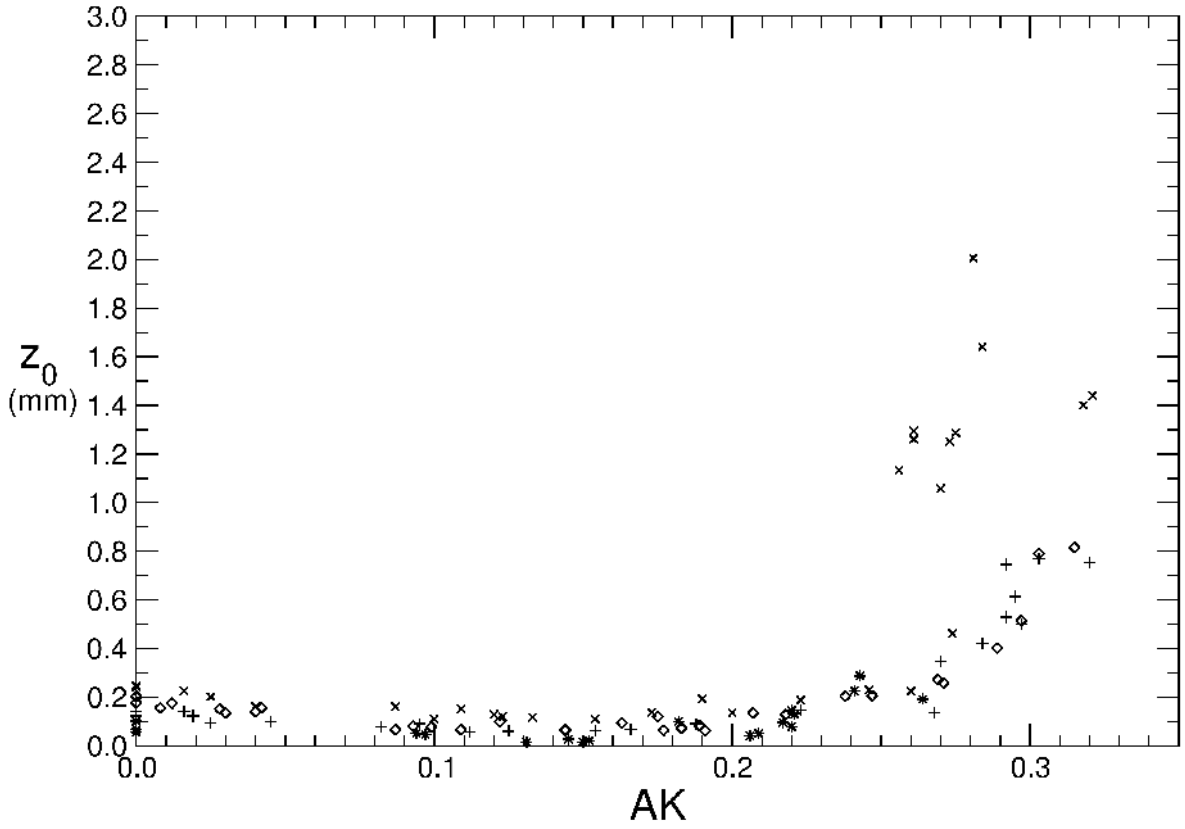

WRL Report No. 223	z0 as a function of AK for each test	Figure 12 Figures050217.sxw

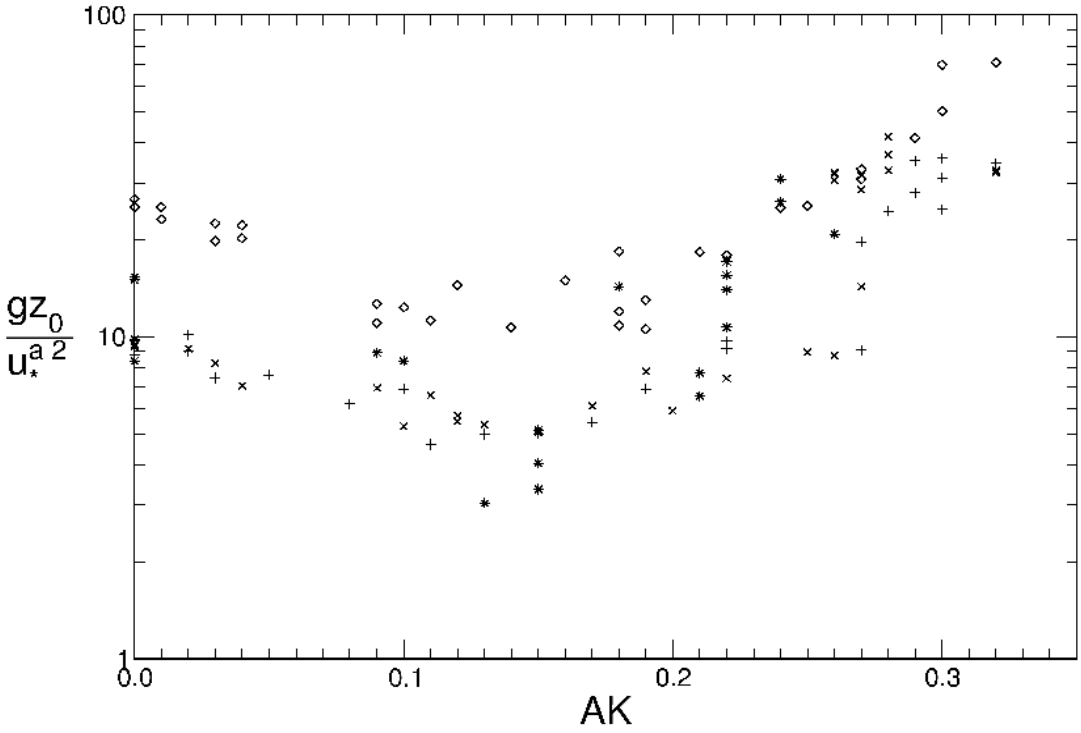

WRL Report No. 223	Charnock parameter as a function of AK for each test	Figure 13 Figures050217.sxw

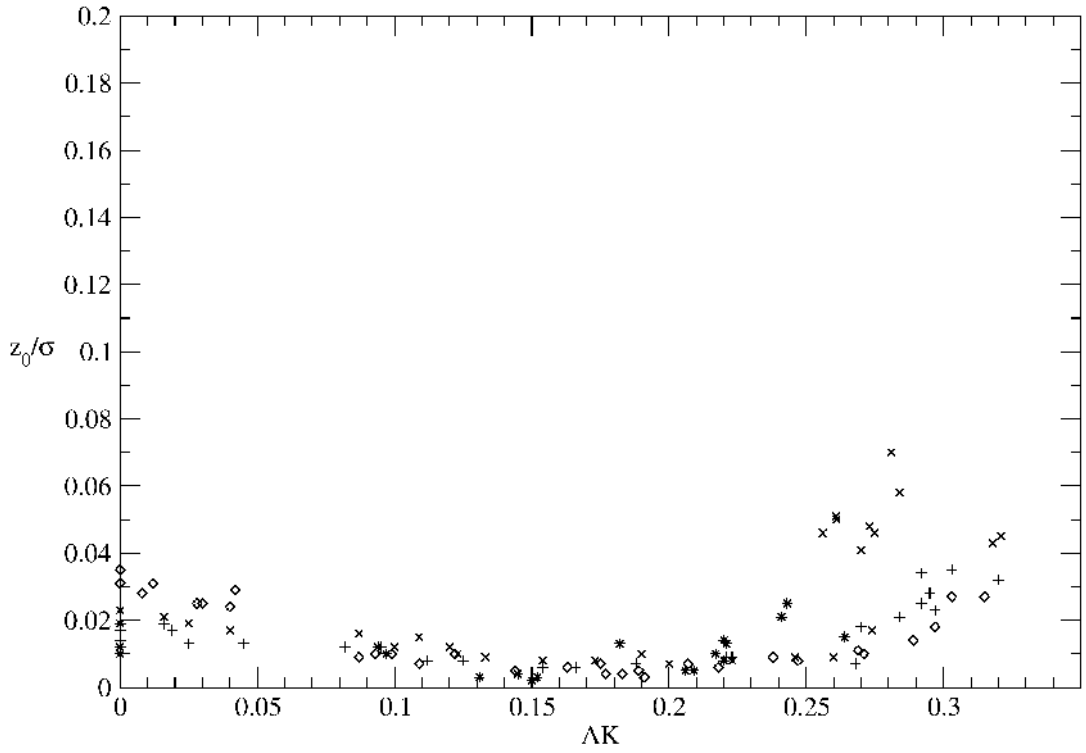

WRL Report No. 223	Ratio of measured roughness length to root-mean-square elevation as a function of mean swell steepness	Figure 14 Figures050217.sxw

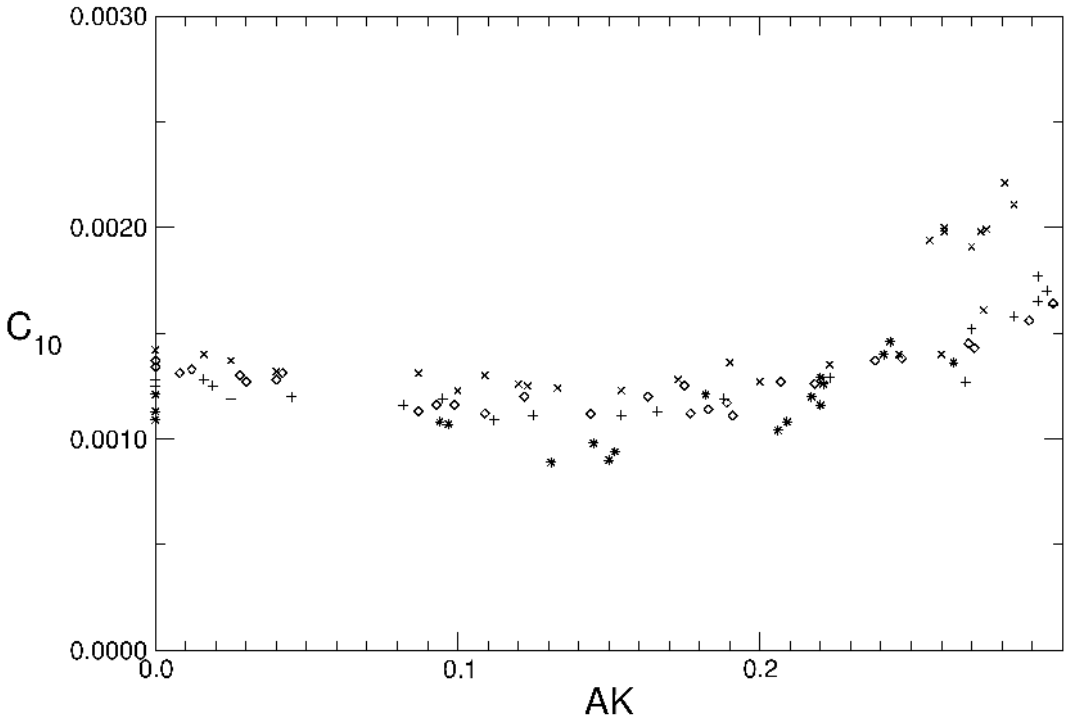

WRL Report No. 223	C10 as a function of AK for each test	Figure 15 Figures050217.sxw

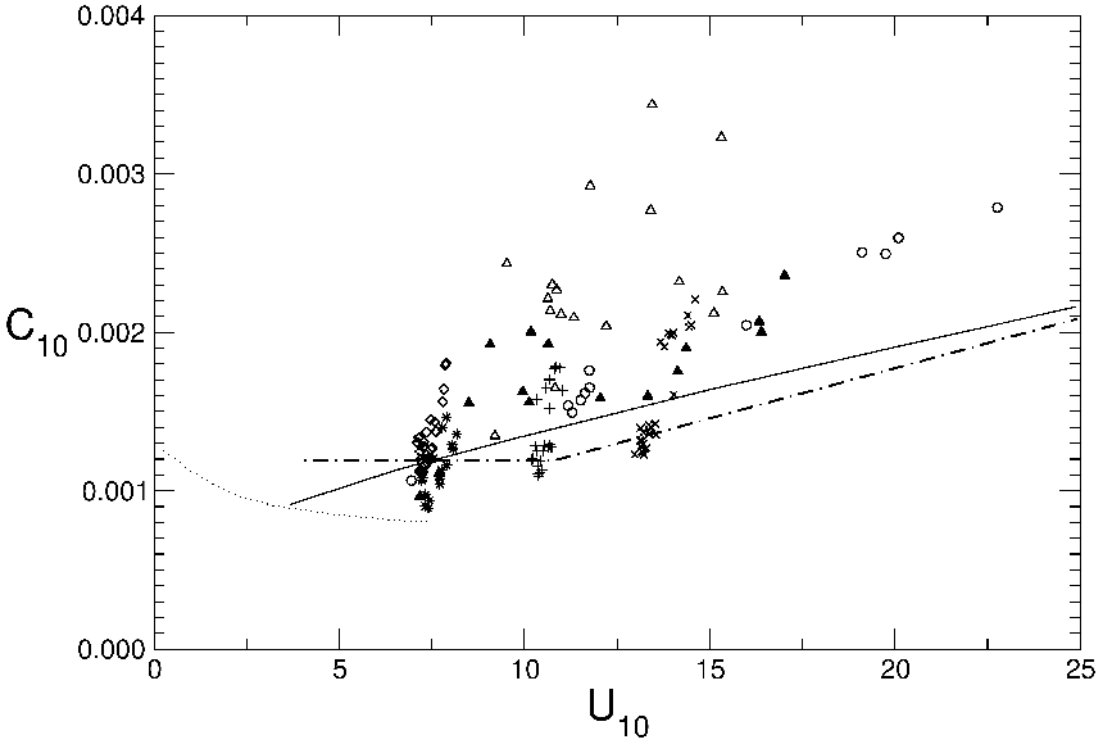

Data from this study as follows: ∗ U=6ms^{-1}, f_s=2.0Hz; + U=8ms^{-1}, f_s=1.6Hz; diamonds U=6ms^{-1}, f_s=1.4Hz; × U=10ms^{-1}, f_s=1.4Hz.

Other data in this figure is taken from Donelan (1990), Figure 4. The dotted line is smooth flow; solid line is Charnock's formula with a coefficient of 0.014; dash-dot line is Large and Pond, 1981. Hollow circles are very young laboratory waves ($6.5 \le U_{10}/c_p \le 15.4$); hollow triangles are young field waves ($3.5 \le U_{10}/c_p \le 4.6$); solid triangles are mature field waves ($0.8 \le U_{10}/c_p \le 2.0$).

WRL Report No. 223	C10 as a function of U10	Figure 16 Figures050217.sxw

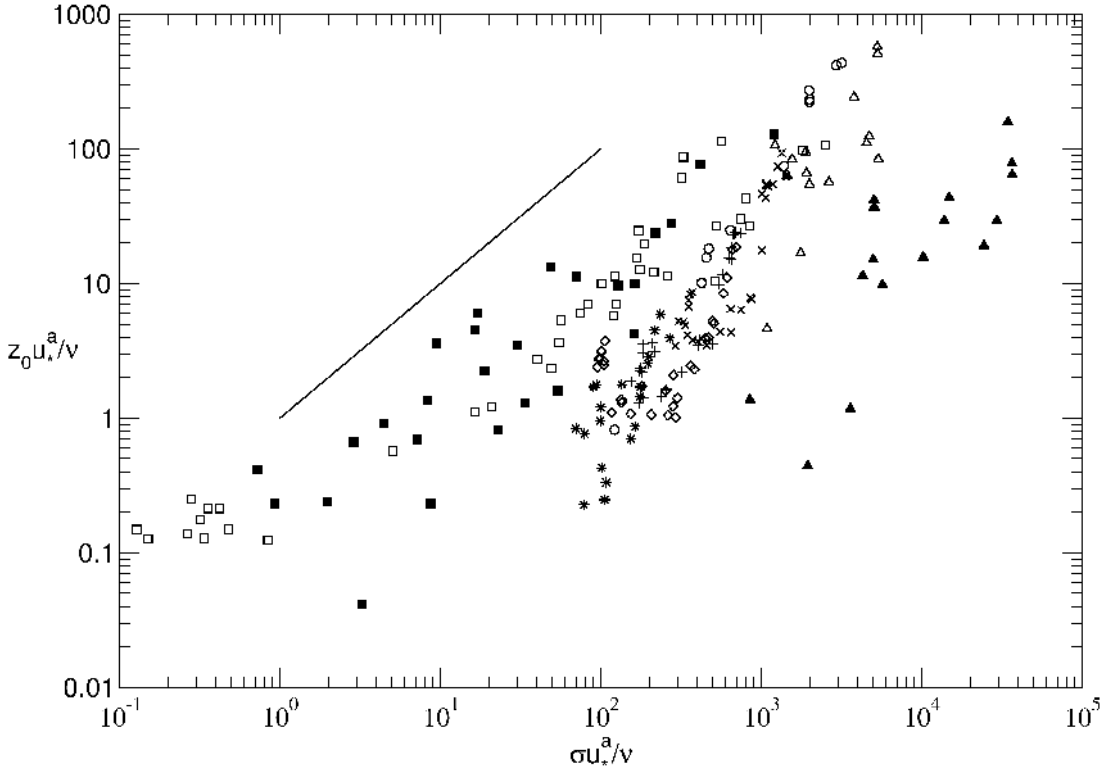

Data from this study as follows: ∗ U=6ms^{-1}, f_s=2.0Hz; + U=8ms^{-1}, f_s=1.6Hz; diamonds U=6ms^{-1}, f_s=1.4Hz; × U=10ms^{-1}, f_s=1.4Hz.

Other data in this figure is taken from Donelan (1990), Figure 11. The slope of the dashed line corresponds to fully rough flow. Hollow squares are laboratory wave experiments by Kunishi, 1963; Solid squares are laboratory wave experiments by Hidy and Plate, 1966; Hollow circles are very young laboratory waves ($6.5 \le U_{10}/c_p \le 15.4$); hollow triangles are young field waves ($3.5 \le U_{10}/c_p \le 4.6$); solid triangles are mature field waves ($0.8 \le U_{10}/c_p \le 2.0$).

WRL Report No. 223	Roughness Reynolds number versus normalised root-mean-square surface elevation	Figure 17 Figures050217.sxw

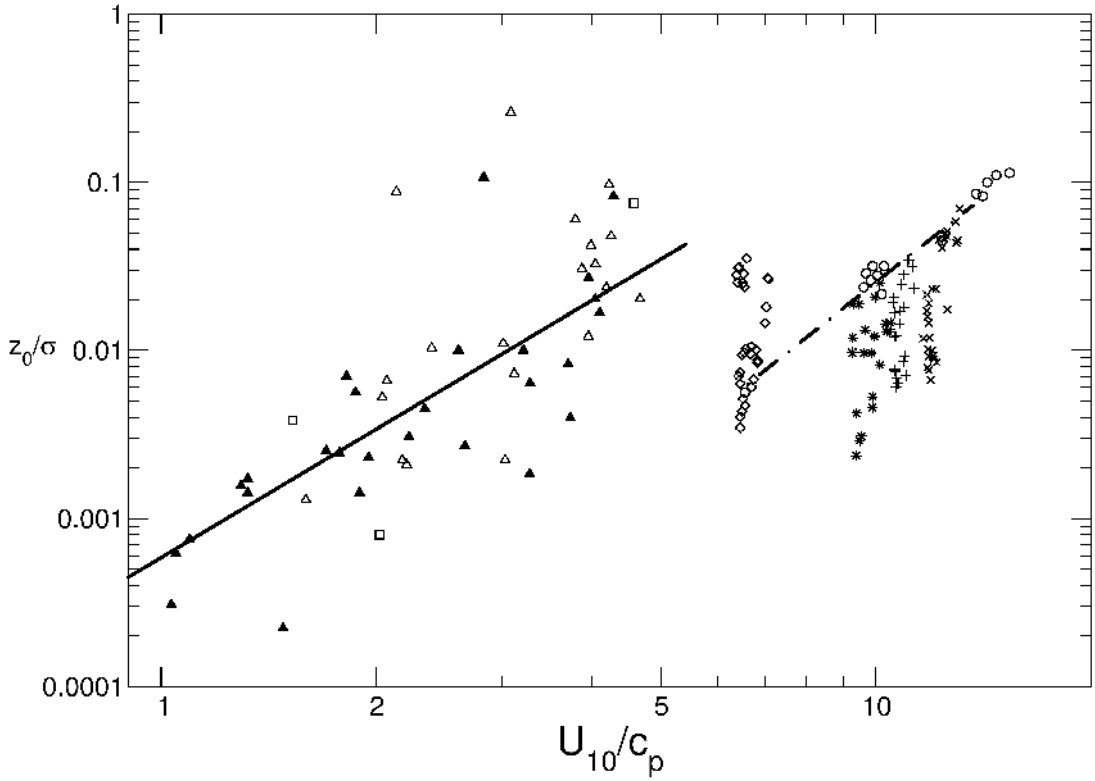

Data from this study as follows: ∗ U=6ms^{-1}, f_s=2.0Hz; + U=8ms^{-1}, f_s=1.6Hz; diamonds U=6ms^{-1}, f_s=1.4Hz; × U=10ms^{-1}, f_s=1.4Hz.

Other data in this figure is taken from Donelan (1990), Figure 11. Hollow circles are young laboratory waves; hollow squares are field data taken with a bulk Richardson number R_b less than 0.002 in magnitude. hollow triangles are field waves with $-0.011<R_b<-0.002$; solid triangles are field waves with $0.002<R_b<0.011$.

WRL Report No. 223	Ratio of measured roughness length to root-mean-square elevation as a function of inverse wave age expressed in terms of U_{10}	Figure 18 Figures050217.sxw

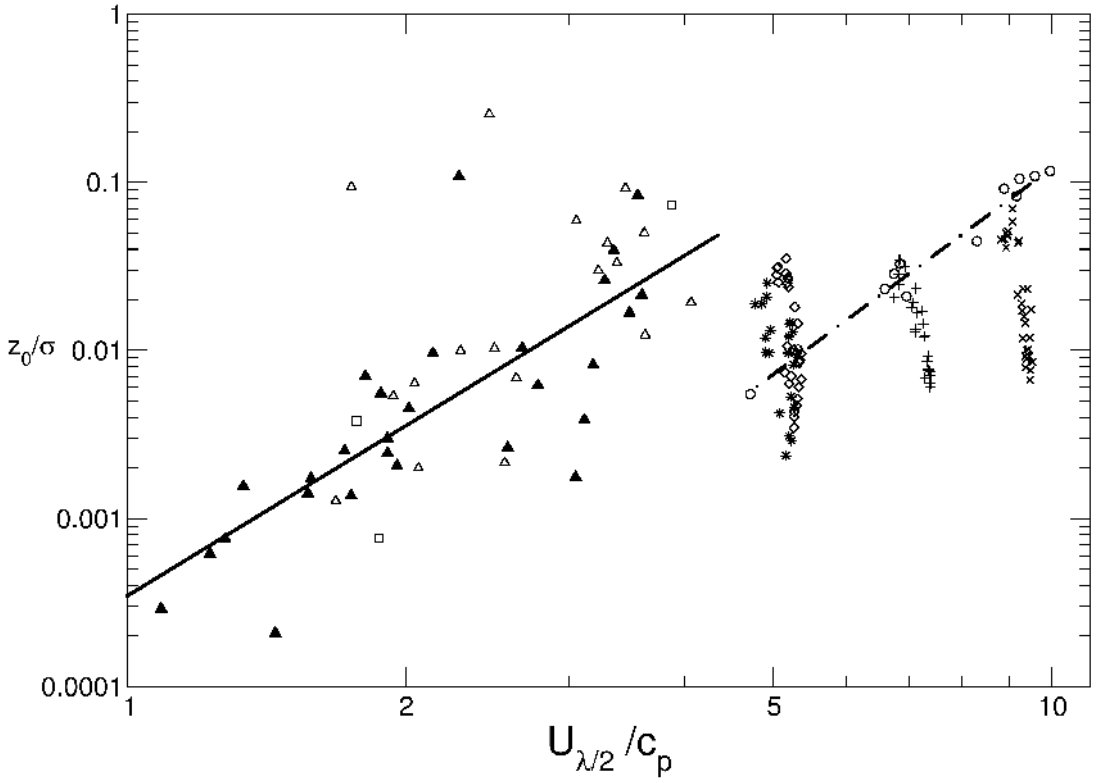

Data from this study as follows: ∗ U=6ms^{-1}, f_s=2.0Hz; + U=8ms^{-1}, f_s=1.6Hz; diamonds U=6ms^{-1}, f_s=1.4Hz; × U=10ms^{-1}, f_s=1.4Hz.

Other data in this figure is taken from Donelan (1990), Figure 11. Hollow circles are young laboratory waves; hollow squares are field data taken with a bulk Richardson number R_b less than 0.002 in magnitude. hollow triangles are field waves with $-0.011<R_b<-0.002$; solid triangles are field waves with $0.002<R_b<0.011$.

WRL Report No. 223	Ratio of measured roughness length to root-mean-square elevation as a function of inverse wave age expressed in terms of $U_{\lambda/2}$	Figure 19 Figures050217.sxw

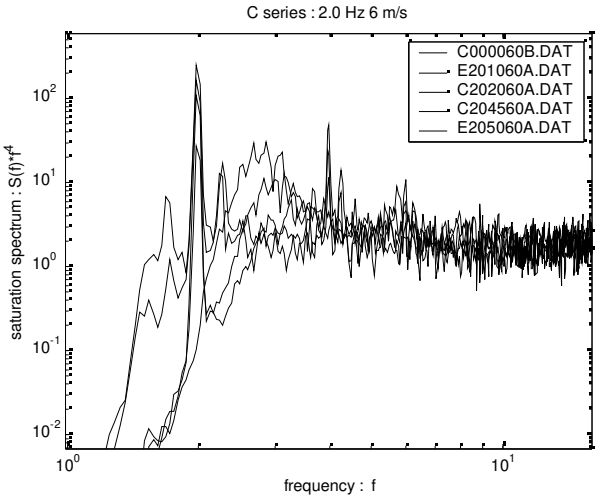

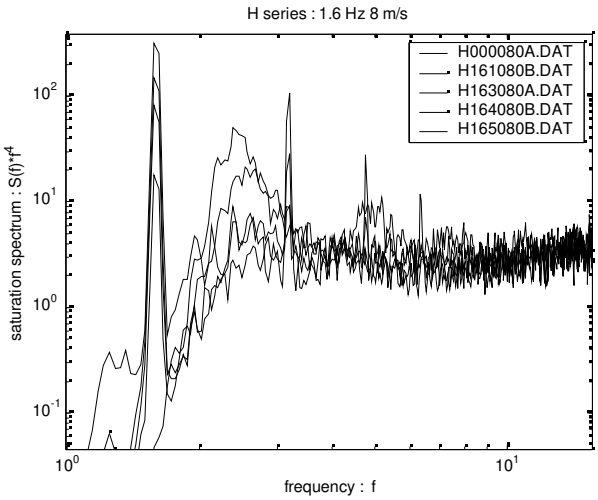

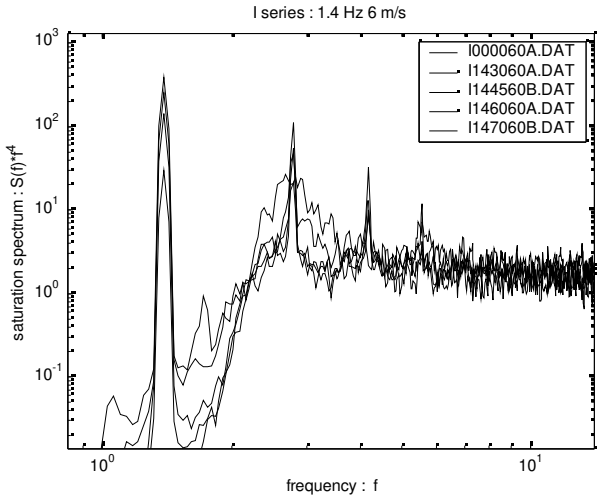

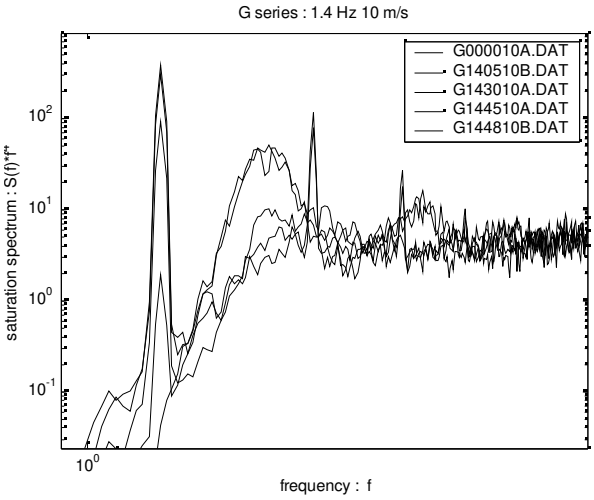

Each panel shows saturation spectra for representative mean swell steepnesses of AK=0.00 , 0.10, 0.15 , 0.20 and 0.25 line styles in legend show are increasing AK from top to bottom.
Top left panel: U=6ms^{-1}, f_s=2.0Hz. Top right: U=8ms^{-1}, f_s=1.6Hz. Lower left : U=6ms^{-1}, f_s=1.4Hz. Lower right: U=10ms^{-1}, f_s=1.4Hz.

Note: saturation units are cm^{2}Hz^{-5}.

WRL Report No. 223	REPRESENTATIVE SATURATION SPECTRA	Figure 20 Figures050217.sxw

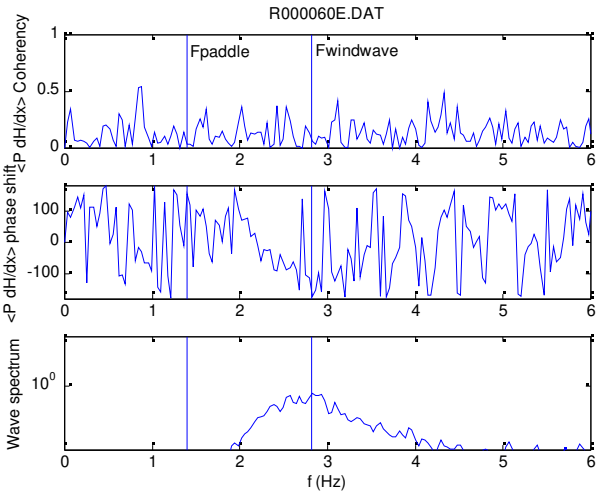

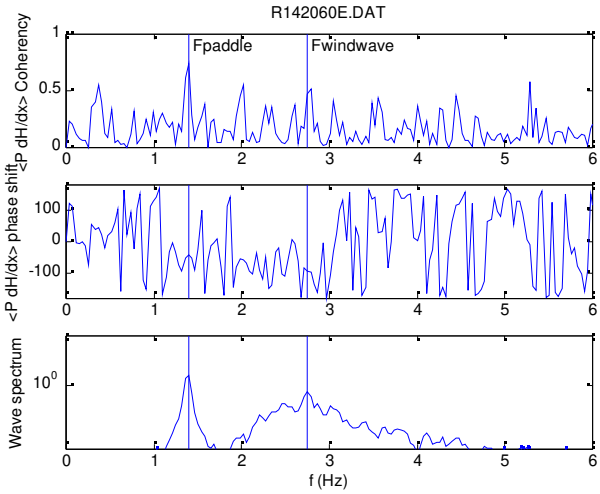

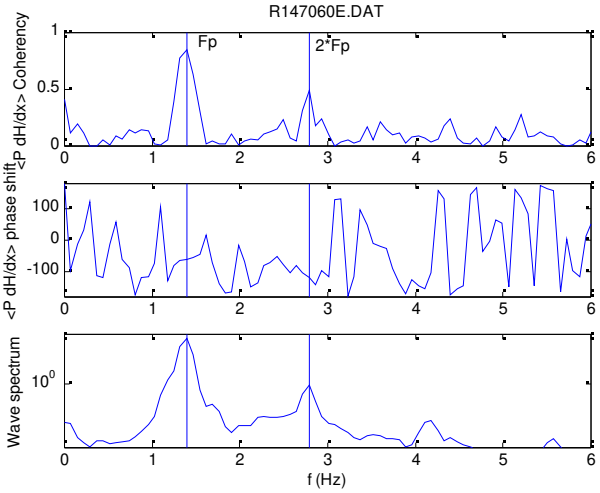

WRL Report No. 223	COHERENCE AND PHASE SPECTRA	Figure 21 Figures050217.sxw

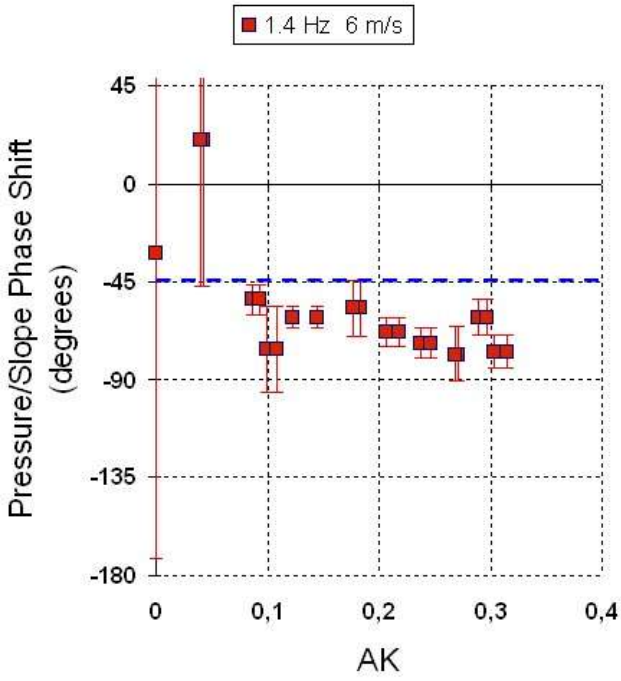

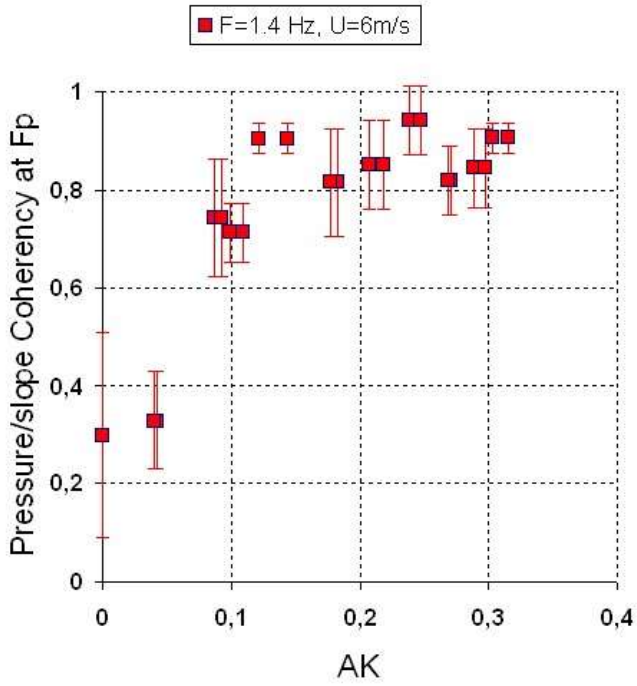

WRL Report No. 223	Phase shift and pressure-slope coherency at f_s	Figure 22 Figures050217.sxw

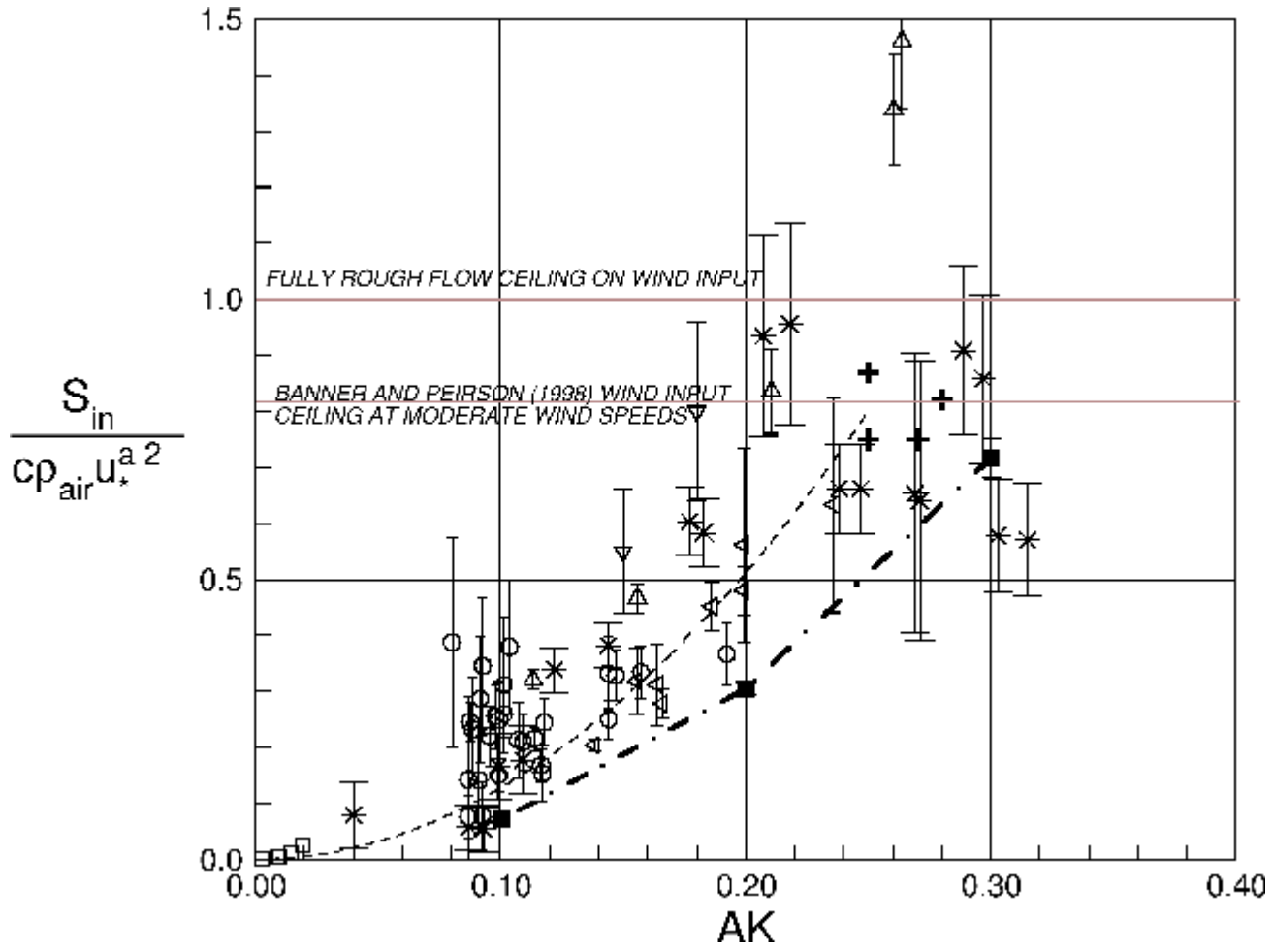

Wind energy input to monochromatic waves normalised by total stress and wave speed as a function of wave steepness in the form proposed by Peirson and Belcher, 2004. Symbols indicate as follows: hollow circles, Bole, 1967; hollow squares, Wilson et al., 1971; + Banner, 1990; triangles to left, Bliven et al., 1986; upright triangles, Mitsuyasu and Honda, 1982; downward triangles, Mastenbroek et al., 1996. Dashed line indicates fitted quadratic relation. Solid squares linked by the dash-dotted line are 2nd order turbulence closure numerical modelling results of Mastenbroek, 1996. * indicate data obtained during this investigation.

WRL Report No. 223	Normalised energy input as a function of AK	Figure 23 Figures050217.sxw